

Pressure-to-depth conversion models for metamorphic rocks: derivation and applications

Arthur Bauville¹ and Philippe Yamato²

¹Japan Agency for Marine-Earth Sciences and Technology

²Univ Rennes, CNRS, Géosciences Rennes - UMR 6118

November 26, 2022

Abstract

Pressure-to-depth conversion is a crucial step towards geodynamic reconstruction but remains strongly debated. Here, we derive pressure-to-depth conversion models using either one or two pressure data points in conjunction. In the two-point method, we assume that both peak and retrograde pressure are recorded at the same depth. This method reduces the depth estimate uncertainty dramatically. We apply the proposed pressure-to-depth conversions to a large set of P data from (ultra)high-pressure metamorphic rocks. We explore different cases to explain the transition from peak to retrograde pressure by varying the direction and magnitude of stress components. Our results show that (1) even small deviatoric stresses have a significant impact on depth estimates, (2) the second principal stress component σ_2 plays an essential role, (3) several models can explain the P evolution of the data but lead to different depth estimates, and (4) strain data offer a means to falsify two-point models. The most commonly used pressure-to-depth conversion method uses one pressure point and the assumption that pressure is lithostatic. Then, the transition from peak to retrograde pressure is interpreted as the result of deep subduction (>100 km), followed by fast exhumation to mid-crustal depth. We show that alternative models where a change in the stress state at a constant depth triggers the pressure transition explain the data equally well. The predicted depth is then shallower than the crustal root Moho (<75 km) for all data points.

Pressure-to-depth conversion models for metamorphic rocks: derivation and applications

Arthur Bauville¹, Philippe Yamato^{2,3}

¹Japan Agency for Marine-Earth Science and Technology, 3173-25, Showa-machi, Kanazawa-ku,
Yokohama-city, Kanagawa, 236-0001, Japan

²Univ Rennes, CNRS, Géosciences Rennes UMR 6118, Rennes, France

³Institut Universitaire de France (IUF), Paris, France

Key Points:

- We present and apply different pressure-to-depth conversion models to a dataset of metamorphic pressure.
- The lithostatic pressure assumption results in an upper estimate of depth at peak pressure (> 100 km).
- A change in stress state < 75 km can trigger a peak to retrograde P decrease and is consistent with the data.

Corresponding author: Arthur Bauville, abauville@jamstec.go.jp

Abstract

Pressure-to-depth conversion is a crucial step towards geodynamic reconstruction but remains strongly debated. Here, we derive pressure-to-depth conversion models using either one or two pressure data points in conjunction. In the two-point method, we assume that both peak and retrograde pressure are recorded at the same depth. This method reduces the depth estimate uncertainty dramatically. We apply the proposed pressure-to-depth conversions to a large set of P data from (ultra)high-pressure metamorphic rocks. We explore different cases to explain the transition from peak to retrograde pressure by varying the direction and magnitude of stress components. Our results show that (1) even small deviatoric stresses have a significant impact on depth estimates, (2) the second principal stress component σ_2 plays an essential role, (3) several models can explain the P evolution of the data but lead to different depth estimates, and (4) strain data offer a means to falsify two-point models. The most commonly used pressure-to-depth conversion method uses one pressure point and the assumption that pressure is lithostatic. Then, the transition from peak to retrograde pressure is interpreted as the result of deep subduction (> 100 km), followed by fast exhumation to mid-crustal depth. We show that alternative models where a change in the stress state at a constant depth triggers the pressure transition explain the data equally well. The predicted depth is then shallower than the crustal root Moho (< 75 km) for all data points.

Plain Language Summary

During the formation of mountain belts, rocks are buried deep in the Earth and then exhumed. In this journey, rocks undergo transformations that record the pressure. We use the pressure to estimate the depth at which a rock was buried to reconstruct the history of mountain belts. The pressure is the sum of the weight of the overlying column of rock and tectonic forces. However, since tectonic forces cannot be measured, there has been a long-standing debate on how much they influence the record of pressure in rocks. Here, we use mathematics and computer code to recalculate the burial depth of a set of rock from pressure data. Two extreme scenarios emerge: (1) when ignoring tectonic forces (classical approach), we interpret the pressure history as the result of deep burial (up to 160 km) followed by fast exhumation (1–10 cm/yr) to approximately 20 km. The mechanism of such fast exhumation is itself intensely debated; (2) when considering tectonic forces, an alternative scenario is that the rock was buried to an intermediate depth (< 75 km), followed by a change in tectonic forces without exhumation. If this second scenario is verified, then the current history of mountain belts must be re-evaluated.

1 Introduction

Geodynamic reconstructions presenting cross-sections, maps, or elaborate large-scale plate reconstructions over time are essential to conceptualize lithospheric processes such as subduction or mountain building and to reconstruct Earth's history. These geodynamic reconstructions are based on quantitative data obtained with a wide range of techniques from field mapping to geophysical imaging. Among these data, pressure-temperature-time-deformation ($P - T - t - \epsilon$) paths obtained from petrological, geochronological, and mineral deformation studies constitute key constraints. These features are indeed the only way to estimate the burial, temperature and deformation evolution of a piece of rock and, by extension, of the geological unit to which it belongs. In particular, estimated depths, in conjunction with geochronological data, are used to reconstruct the formation process of orogens (e.g., Chopin, 2003; Ernst et al., 2007; Agard et al., 2009).

The conversion of pressure to depth is crucial in establishing a geodynamic reconstruction based on petrographic data. Depth can be retrieved from the lithostatic pres-

sure P_{litho} , i.e., the weight of the overlying column of rock, by the formula:

$$z = \frac{P_{litho}}{\rho g}, \quad (1)$$

where ρ is the average density of the rock column, g is the gravitational acceleration and z is depth. However, P_{litho} cannot be directly estimated from metamorphic rocks; instead, we can estimate the mean stress, also called the pressure, P (Moulas et al., 2019). Therefore, an additional step is required to relate P to P_{litho} . This additional step involves information about the three-dimensional deviatoric stress state responsible for rock deformation. Unfortunately, deviatoric stresses cannot be measured, and one must, therefore, make assumptions regarding the stress state to retrieve P_{litho} . Depending on the assumption made, the final depth estimate can vary by more than a factor of two. Since these crucial assumptions are hard or maybe impossible to falsify, there has been a long-standing debate over (1) what is the most adequate stress state assumption to use for pressure-to-depth conversion, (2) how deeply were metamorphic rocks buried, and (3) how are metamorphic rocks exhumed (e.g., Jamieson, 1963; Ernst, 1963; Brace et al., 1970; Mancktelow, 1993; Godard, 2001; Green, 2005; Agard et al., 2009; Wheeler, 2014; B. Hobbs & Ord, 2015; Wheeler, 2014; Tajčmanová, 2015; Moulas et al., 2013; Gerya, 2015; B. E. Hobbs & Ord, 2017; Moulas et al., 2019; Schmalholz & Podladchikov, 2014; Yamato & Brun, 2017; Reuber et al., 2016; Schenker et al., 2015).

The most common assumption is to ignore deviatoric stresses because metamorphic rocks are assumed to be weak at the depths considered (e.g., Guillot et al., 2009; Agard et al., 2009; Beltrando et al., 2007; Rubatto et al., 2011). Thus, $P = P_{litho}$ and one can readily use eq. 1. We call this assumption the "lithostatic case". In a rock, the magnitude of deviatoric stresses can vary from zero to the point of rock failure. Hence, the mean deviatoric stress can be of a magnitude comparable to lithostatic pressure, and P can vary from 1 to 2 times the value of P_{litho} in compression for a homogeneous rock (Petrini & Podladchikov, 2000). The difference between P and P_{litho} is referred to as "tectonic pressure" (Mancktelow, 2008), "tectonic overpressure" (Mancktelow, 1993; Schmalholz & Podladchikov, 2013) or simply "overpressure" when it is positive or "underpressure" when it is negative (Moulas et al., 2013). Note that the overpressure model is a general model of which the "lithostatic case" constitutes one special case. Therefore, it is essential to consider variations in the stress state when interpreting pressure-temperature ($P - T$) paths.

In most cases, the $P - T$ evolution of a (U)HP metamorphic rock can be approximated by three linear segments. A prograde segment (highlighted in blue in Fig. 1A) that shows increases in both P and T and a retrograde part (in green in Fig. 1A) divided in two segments: a retrograde *stage 1* and a retrograde *stage 2* (see Fig. 1A). The first stage of the retrograde path generally shows a large decrease in pressure and only minor variations in temperature, while the second stage presents decreases in both pressure and temperature conditions (Yamato 2017). Hereafter, we use the notations P_p and T_p to refer to the pressure and temperature conditions at the peak of (U)HP metamorphism (time t_1 in Fig. 1A), respectively. Similarly, P_r and T_r refer to the pressure and temperature conditions at the end of retrograde *stage 1* (time t_2 in Fig. 1A).

There are arguably two events in the $P - T$ path that cause most of the debate: peak metamorphism (P_p, T_p) and retrograde *stage 1* (i.e., the transition from P_p to P_r). Thermobarometric studies often provide P_p, T_p and P_r, T_r , sometimes in association with geochronological dating. We present the dataset of $P_p, T_p - P_r, T_r$ collected from the literature in the $P - T$ space in Figure 1B and in the space $P_p - P_r$ in Figure 1C. In $P_p - P_r$ space, most data points are contained within a fan centered on 0, which suggests that P_p and P_r are proportional, with coefficients of proportionality, P_p/P_r , between 2.4 and 4.8. A few data points with values $P_p < 1.5$ have a coefficient of proportionality < 2.4 as low as 1.4. We term these points "Others (outliers)".

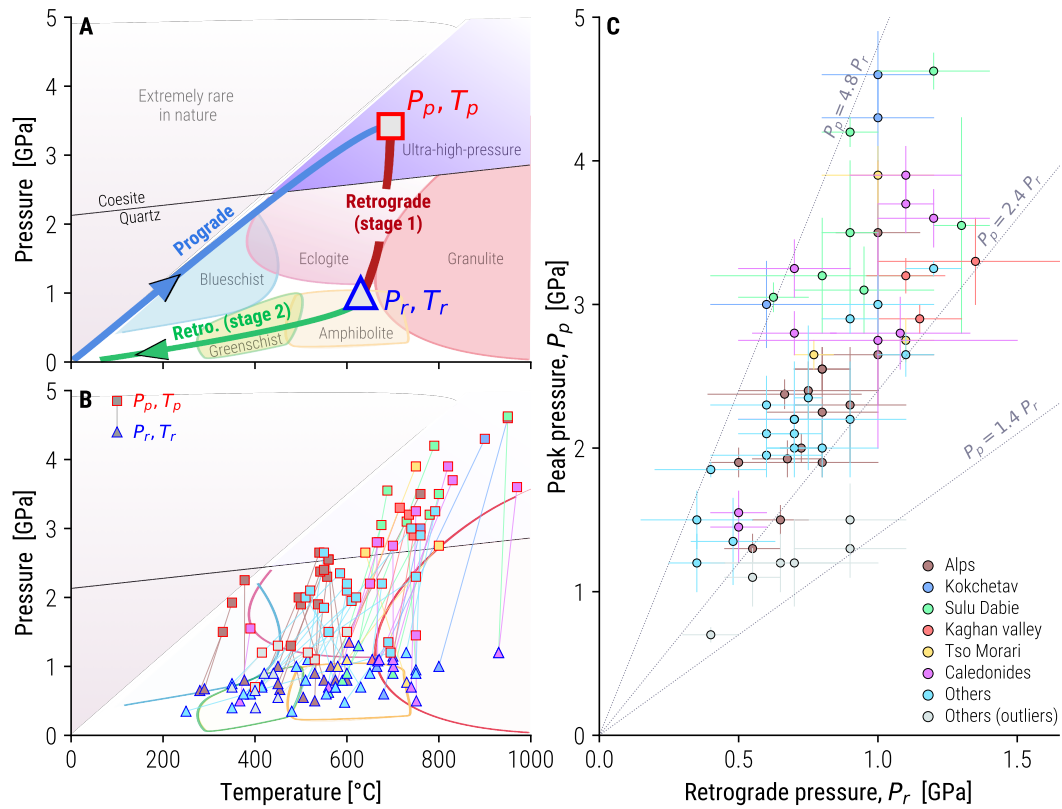


Figure 1. (A) Typical example of a $P - T$ path. (B) Dataset in $P - T$ space. Colors correspond to the orogenic system from which data come as presented in C. (C) Repartition of the data (see Suppl. Mat. for references) in a P_p vs. P_r diagram

110 To illustrate the consequence of stress state assumptions on geodynamic interpre-
 111 tations, let us consider a rock presenting a mineral paragenesis equilibrated at 3.0 GPa.
 112 This rock can be interpreted as having been buried up to 100 km depth under the "litho-
 113 static" assumption (using $\rho = 3000 \text{ kg/m}^3$ and $g = 10 \text{ m/s}^2$) but only approximately
 114 50 km when considering a magnitude of deviatoric stresses close to the brittle yield stress
 115 in compression. While the former corresponds to mid-lithospheric depth, the latter would
 116 correspond to crustal-root depth. Pleuger and Podladchikov (2014), for example, pro-
 117 posed a geodynamic reconstruction of the central Alps based on structural arguments
 118 wherein the Adula nappe, an eclogite-bearing metamorphic unit in the Alps, was buried
 119 to 50-60 km depth. This depth estimate implies an overpressure of 40-80 % of the litho-
 120 static pressure and suggests that the burial and exhumation of this unit occurred within
 121 an orogenic crustal wedge. In alternative models using the "lithostatic assumption", the
 122 nappe was buried to 80 km depth during subduction and then rapidly exhumed by slab
 123 breakoff (S. M. Schmid et al., 1996; Froitzheim et al., 2003) or subvertical extreme thin-
 124 ning (Nagel, 2008). The scenario of S. M. Schmid et al. (1996) employs one subduction
 125 zone in conjunction with a normal fault, while the models of (Froitzheim et al., 2003)
 126 and Nagel (2008) involve two subduction zones. Thus, different assumptions regarding
 127 pressure-to-depth conversion lead to different interpretations of the process of mountain
 128 building. Therefore, it is crucial to understand, compare, and evaluate the implications
 129 of different assumptions about the stress state when designing geodynamic reconstruc-
 130 tions.

131 Retrograde *stage 1*, when the pressure decreases from P_p to P_r in a relatively short
 132 amount of time, is also at the center of heated debate. Using the "lithostatic assump-
 133 tion", the transition from P_p to P_r is interpreted as an exhumation event. In conjunc-
 134 tion with dating data, this phase of exhumation is generally interpreted as fast, with ex-
 135 humation rates comparable to subduction rates (1-10 *cm/yr*) (e.g., Rubatto & Hermann,
 136 2001; Parrish et al., 2006). Various mechanisms have been proposed to explain these fast
 137 exhumation rates, such as buoyancy-driven exhumation (Wheeler, 1991; Beaumont et
 138 al., 2009; Butler et al., 2013, 2014; E. Burov et al., 2014; Schmalholz & Schenker, 2016),
 139 slab breakoff (Huw Davies & von Blanckenburg, 1995), normal faulting (Platt, 1986; Ring
 140 et al., 1999; S. M. Schmid et al., 1996), rollback (Brun & Faccenna, 2008), or channel
 141 flow (e.g., Guillot et al., 2009). These and other mechanisms are discussed in detail in
 142 several reviews (Guillot et al., 2009; B. R. Hacker & Gerya, 2013; Warren, 2013). In con-
 143 trast to the fast exhumation interpretation, Yamato and Brun (2017) showed that when
 144 considering the large deviatoric stresses assumption, the transition from P_p to P_r can
 145 be explained, for many rock samples, by a switch from a compressional to an extensional
 146 stress state without exhumation.

147 In this contribution, we first review the mathematical background of pressure and
 148 stress. Then, we formulate a "one-point method" of pressure-to-depth conversion to es-
 149 timate depth based on a single pressure data point and a "two-point method" that uses
 150 both P_p and P_r with the assumption that $z_p = z_r$. We apply these methods to our dataset
 151 (Fig. 1B) to determine an estimated depth range for each sample. Finally, we discuss
 152 the consequences of different assumptions for geodynamic interpretation and point out
 153 ways of falsifying some assumptions. Our goal is both to raise awareness about the is-
 154 sue of pressure-to-depth conversion and to provide tools allowing one to perform such
 155 conversion easily. For this reason, we provide computer codes (Jupyter notebooks) as
 156 supplementary information S2-S10. These scripts allow readers to reproduce most of the
 157 figures presented in this article readily and to extend the database with their own data.
 158 The codes can also be used to experiment with stress states and material properties.

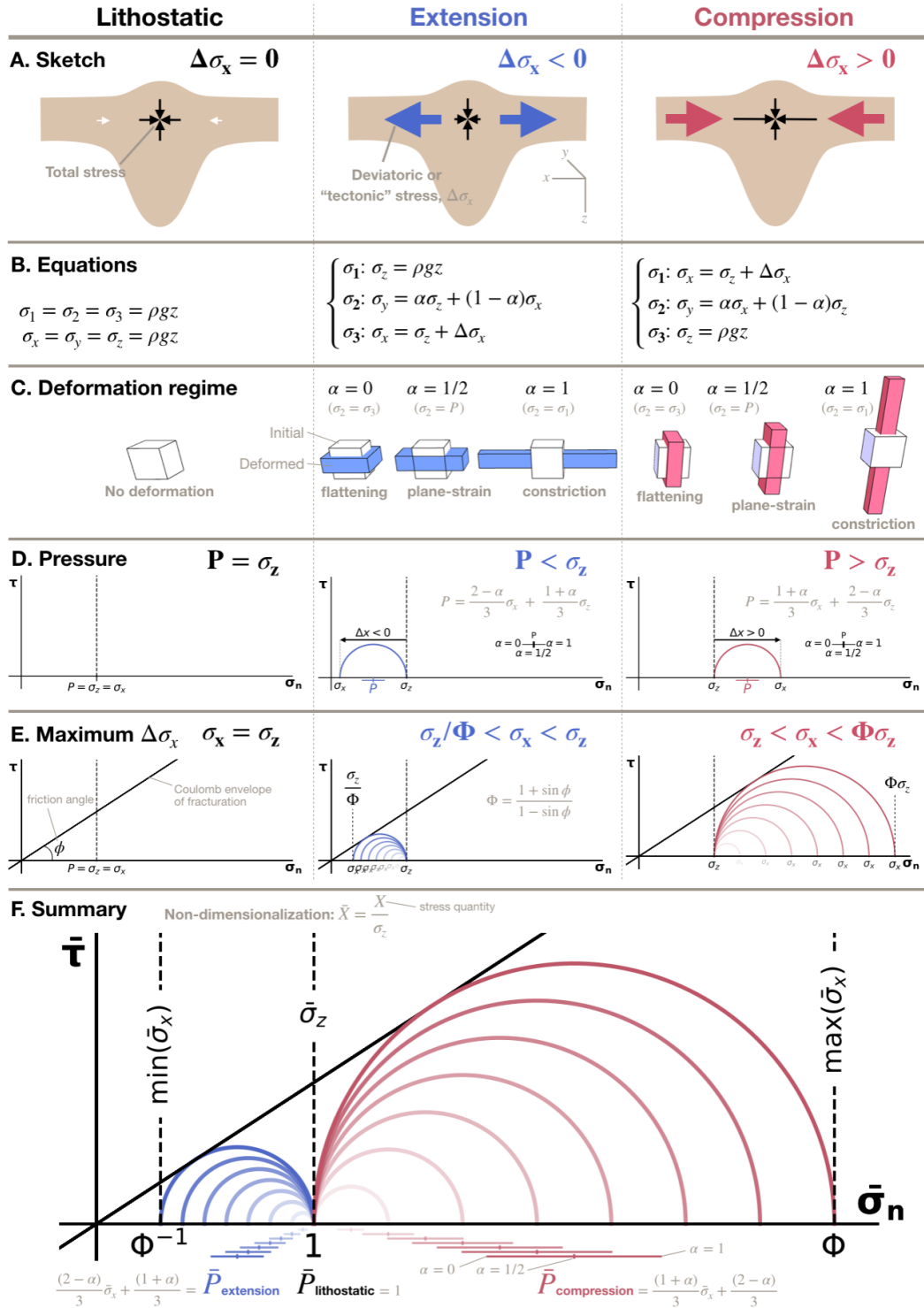


Figure 2. Overview of the principal characteristics of the model and definitions. See text for details concerning notation. $\Delta\sigma_x$ corresponds to the stress magnitude applied in the x -direction. Graphics presenting σ_n vs. τ (i.e., normal stress vs. shear stress) correspond to Mohr diagrams.

2 One-point method of pressure-to-depth conversion

2.1 Overview of the model

2.1.1 Sketch, coordinate system and equations of stress

Let us consider an ideal and simplified orogen submitted to horizontal tectonic stresses in a three-dimensional Cartesian orthonormal system (x, y, z) where z is vertical and points downward and x is the direction in which tectonic loading is applied (Fig. 2A). $\sigma_x, \sigma_y, \sigma_z$ are the normal components of the stress tensor in this coordinate system, and $\sigma_1, \sigma_2, \sigma_3$ are the principal stresses. We use the convention that stresses are positive in compression. We assume, in a first step, that the stress state is Andersonian, that is, one principal stress direction is vertical, and the other two are horizontal (Anderson, 1905). We fix the y -axis in the direction of σ_2 . Thus, we only consider cases where the stress state can induce normal or reverse faulting, and we ignore the stress states that would result in strike-slip faulting. Under these assumptions, the total vertical stress σ_z corresponds to the weight of the column of rock above the considered point (or P_{litho}) and is given by:

$$\sigma_z = \rho g z, \quad (2)$$

where ρ is the density of the overlying rocks, g is the gravitational acceleration and z is the depth where the computation is performed. When a tectonic stress of magnitude $\Delta\sigma_x$ is applied in the x -direction, the following equation applies:

$$\sigma_x = \sigma_z + \Delta\sigma_x \quad (3)$$

Three tectonic regimes can be considered depending on the horizontal loading condition (Fig. 2A): (1) lithostatic, when $\Delta\sigma_x = 0$; (2) compression, when $\Delta\sigma_x > 0$; (3) extension, when $\Delta\sigma_x < 0$. Equations describing the stress state for these three tectonic regimes are presented in Figure 2B.

2.1.2 Deformation

The magnitude of the deformation is proportional to $\Delta\sigma_x$, and the direction of maximum stretch is parallel to the direction of σ_3 . Thus, there is no deformation in the lithostatic case, and the maximum stretch is horizontal in the extensional case and vertical in the compressional case. The total stress in the y -direction is always $\sigma_y = \sigma_2$, and we use the variable α that ranges between 0 and 1 to describe σ_2 as a function of σ_1 and σ_3 such that:

$$\sigma_2 = \alpha\sigma_1 + (1 - \alpha)\sigma_3. \quad (4)$$

Figure 2C shows how α is related to the mode of deformation. When $\alpha = 0$, $\sigma_2 = \sigma_3$ (see eq. 4), and the rock deforms by flattening. When $\alpha = 1$, $\sigma_2 = \sigma_1$, and the rock deforms by constriction. When $\alpha = 0.5$, $\sigma_2 = (\sigma_1 + \sigma_3)/2 = P$, and the deformation is plane strain.

2.1.3 Pressure

By definition, pressure (P) corresponds to the isotropic part of the stress tensor and, in principal stress coordinates, it can be expressed as follows:

$$P = \frac{\sigma_1 + \sigma_2 + \sigma_3}{3}. \quad (5)$$

Hence, $P = \sigma_z$ in the lithostatic case, $P < \sigma_z$ in extension (because $\Delta\sigma_x < 0$), and $P > \sigma_z$ in compression (because $\Delta\sigma_x > 0$). The Mohr diagrams in Figure 2D illustrate these relationships. In the diagrams, the horizontal and vertical axes represent the

normal stress σ_n and shear stress τ on planes within the rock mass, respectively. Pressure is represented by a cross symbol, where the central vertical bar represents the value of pressure when the rock deforms under plane-strain conditions ($\alpha = 1/2$) and the horizontal bar represents the range of pressure associated with values of α between 0 (flattening) and 1 (constriction). The equation for P as a function of α is obtained by substituting eq. (4) into eq. (5), which yields

$$P = \frac{(1 + \alpha)}{3}\sigma_1 + \frac{(2 - \alpha)}{3}\sigma_3. \quad (6)$$

172

2.1.4 *Limit of stress and rock failure*

When tectonic loading is applied, rocks first undergo elastic or viscous deformation. Stress loading can be increased up to the point where the rock breaks. At this point, the maximum stresses on a given plane within the rock are given by the Mohr-Coulomb law as:

$$\tau = \tan \phi \sigma_n, \quad (7)$$

where ϕ is the friction angle. Rock experiments show that $\phi \approx 30^\circ$ for most rock types (Byerlee, 1978). To simplify the derivation, we ignore cohesion since it is small (order of 10 – 50 MPa) compared to the pressure of metamorphic rocks considered here (order of GPa). The supplementary scripts (supplementary information S2 to S10) also allow the reader to reproduce most figures in this publication while taking cohesion into account (see Yamato and Brun (2017) for the derivation). Mohr's circle is defined by

$$\sigma_n = \frac{\sigma_1 + \sigma_3}{2} - \frac{\sigma_1 - \sigma_3}{2} \sin \phi \quad (8)$$

and

$$\tau = \frac{\sigma_1 - \sigma_3}{2} \cos \phi. \quad (9)$$

Substituting eq. (8) and eq. (9) into eq. (7) yields

$$\sigma_1 = \Phi \sigma_3, \text{ with} \quad (10)$$

$$\Phi = \frac{1 + \sin \phi}{1 - \sin \phi}. \quad (11)$$

173

Figure 2E illustrates the possible stress states associated with different tectonic regimes. This figure presents the whole range of possibilities from the "lithostatic" case to the brittle case.

174

175

176

In extension, $\sigma_x = \sigma_3$, and $\sigma_z = \sigma_1$; therefore, the minimum total horizontal stress is $\min(\sigma_x) = \sigma_z/\Phi$ (Fig. 2E, middle panel). Conversely, in compression, $\sigma_x = \sigma_1$, and $\sigma_z = \sigma_3$; therefore, the maximum total horizontal stress is $\max(\sigma_x) = \Phi \sigma_z$ (Fig. 2E, right panel). The quantity $(\sigma_1 - \sigma_3)/2$, i.e., the radius of the Mohr circle, is also called the second invariant of the deviatoric stress tensor or the "magnitude of deviatoric stresses".

177

178

179

180

181

2.1.5 *Summary*

Finally, Figure 2F presents a Mohr-Coulomb diagram that summarizes the discussion to this point. The diagram is presented in a non-dimensional form where the overbar indicates that a quantity is normalized by σ_z (e.g., $\bar{\sigma}_x = \sigma_x/\sigma_z$). The pressure in the lithostatic case, or lithostatic pressure, is equal to σ_z (i.e., the weight of the column of rocks). The nondimensional lithostatic pressure is therefore equal to $\bar{\sigma}_z = 1$ (Fig. 2F). In compression, the normalized total horizontal stress $\bar{\sigma}_x$ can vary from 1 (no deformation) to Φ (onset of brittle deformation), and $P > \sigma_z$. In extension, $\bar{\sigma}_x$ can vary

from $1/\Phi$ (brittle deformation) to 1 (no deformation), and $P < \sigma_z$. In these three cases, following eq. (5), the nondimensional pressure \bar{P} can then be written as:

$$\bar{P}_l = 1, \quad (12)$$

$$\bar{P}_e = \frac{2 - \alpha}{3} \bar{\sigma}_x + \frac{1 + \alpha}{3}, \quad (13)$$

$$\bar{P}_c = \frac{1 + \alpha}{3} \bar{\sigma}_x + \frac{2 - \alpha}{3}, \quad (14)$$

where the subscripts c , e , and l relate to the compression, extension and lithostatic tectonic regimes, respectively (see also Fig. 2F). Another useful result is obtained by solving the previous equations for σ_z :

$$\begin{cases} \sigma_z = \frac{3P}{1 + \alpha + \bar{\sigma}_x(2 - \alpha)}, & \text{when } \bar{\sigma}_x \leq 0, \\ \sigma_z = \frac{3P}{2 - \alpha + \bar{\sigma}_x(1 + \alpha)}, & \text{when } \bar{\sigma}_x \geq 0. \end{cases} \quad (15)$$

182

2.2 Pressure-to-depth conversion ratio z/P

To convert metamorphic pressure estimates (P) into depth (z), one can use the simple relation $z = \frac{z}{P}P$, where z/P is the gradient of depth as a function of pressure, which we refer hereafter as the "pressure-to-depth conversion ratio", expressed in km/GPa , and is equal to

$$\frac{z}{P} = \frac{1}{\rho g \bar{P}}, \text{ where} \quad (16)$$

$$\bar{P} = P/\sigma_z. \quad (17)$$

183

184

185

186

187

188

189

190

191

192

193

Figure 3 shows graphs of $1/\bar{P}$ and z/P as a function of the horizontal stresses expressed by $\bar{\sigma}_x$ (horizontal axis) and α (different lines). The graphs were calculated by substituting \bar{P} in eq. (16) with eq. (13) when $\bar{\sigma}_x \leq 1$ (i.e., in extension) or eq. (14) when $\bar{\sigma}_x \geq 1$ (i.e., Panels A to E show Mohr diagrams illustrating the stress state for given values of $\bar{\sigma}_x$). Throughout this article, we use $\rho g = 28000 \text{ kg/m}^2/\text{s}^2$, representing crustal rocks. A value of $\tan(\phi) = 0.6$ is often used in the literature. This value is the result of fitting data from rock friction experiments by Byerlee (1978). In the main article, we use the value $\tan(\phi) = 0.65$ that offers a better fit to the data in the absence of cohesion. The difference has only a negligible influence on pressure estimates. Readers can easily recompute our results using any value of cohesion, ϕ , or ρ by using the scripts provided in the supplementary material (supplementary information S2 to S10).

194

195

196

197

198

199

200

201

202

203

When the pressure is considered lithostatic ($\bar{\sigma}_x = 1$, Fig. 3C), the pressure-to-depth conversion ratio is $z/P = 35 \text{ km/GPa}$. However, this ratio varies significantly when $\bar{\sigma}_x$ increases (compression) or decreases (extension). For example, in the case where $\sigma_2 = \sigma_1$ and $\bar{\sigma}_x$ is minimum, $z/P = 64 \text{ km/GPa}$ (Fig. 3A). In contrast, when $\bar{\sigma}_x$ is maximum, $z/P = 16 \text{ km/GPa}$ (Fig. 3E). Small deviations of $\bar{\sigma}_x$ from 1 have significant impacts on the pressure-to-depth conversion ratio. For example, when the applied tectonic stress $\Delta\bar{\sigma}_x = \min(\Delta\bar{\sigma}_x)/4$, $z/P = 39 \text{ km/GPa}$ (Fig. 3B), and when $\Delta\bar{\sigma}_x = \max(\Delta\bar{\sigma}_x)/4$, $z/P = 25 \text{ km/GPa}$ (Fig. 3D). The value of α also exerts a strong control on the pressure-to-depth conversion ratio, particularly in extension; e.g., when $\bar{\sigma}_x = \Phi^{-1}$, the conversion ratio varies from 45 to 64 km/GPa depending on the value of α .

204

2.3 Application of the one-point method

205

206

207

We now apply the pressure-to-depth conversion ratio derived in the previous section to our dataset of peak (P_p) and retrograde (P_r) metamorphic pressures. Figure 4 shows the depths estimated from this conversion. Depth estimates at peak pressure (z_p)

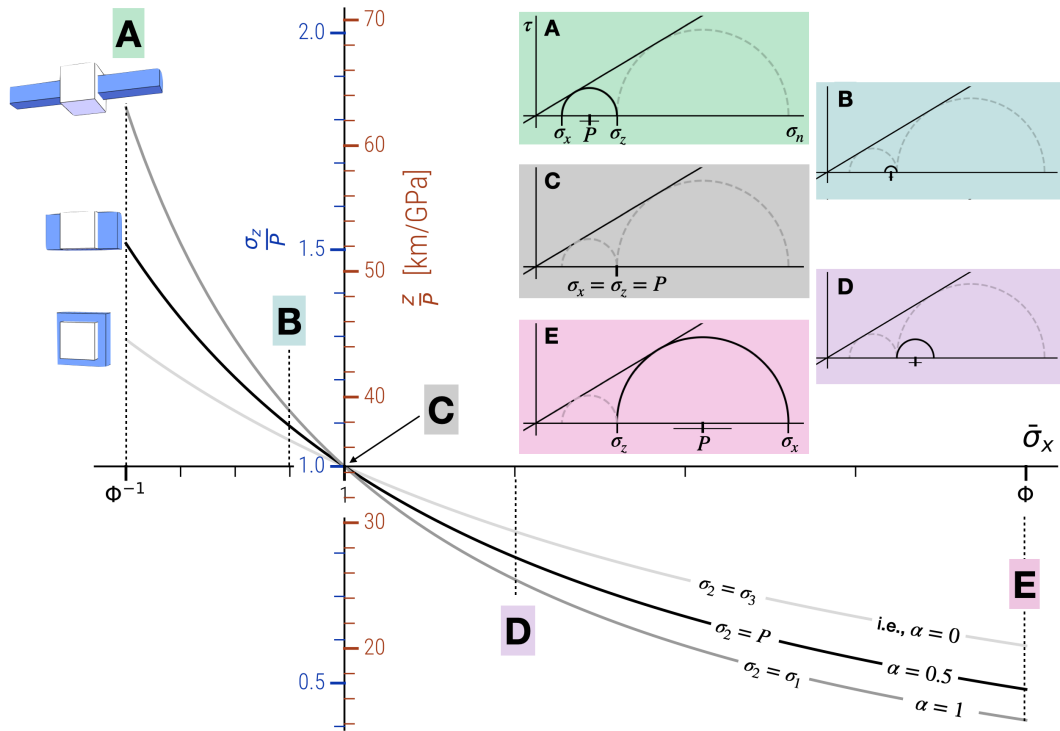


Figure 3. Pressure-to-depth conversion ratio (z/P) as a function of normalized horizontal stress $\bar{\sigma}_x = \sigma_x/\sigma_z$. The vertical axis indicates the ratio of vertical stress to pressure (Sz/P , blue axis) or the pressure-to-depth conversion ratio (z/P , red). We use $\rho g = 28000 \text{ kg/m}^2/\text{s}^2$, and $\tan \phi = 0.65$. The three lines correspond to different values of α (i.e. σ_2). The mode of deformation associated with α is illustrated by the cartoons on the left, where the white and blue boxes represent the undeformed and deformed states, respectively. The Mohr diagrams represent the outer envelope of stress states at points A to E. In these panels, pressure P is represented by a cross, as in figure ??F.

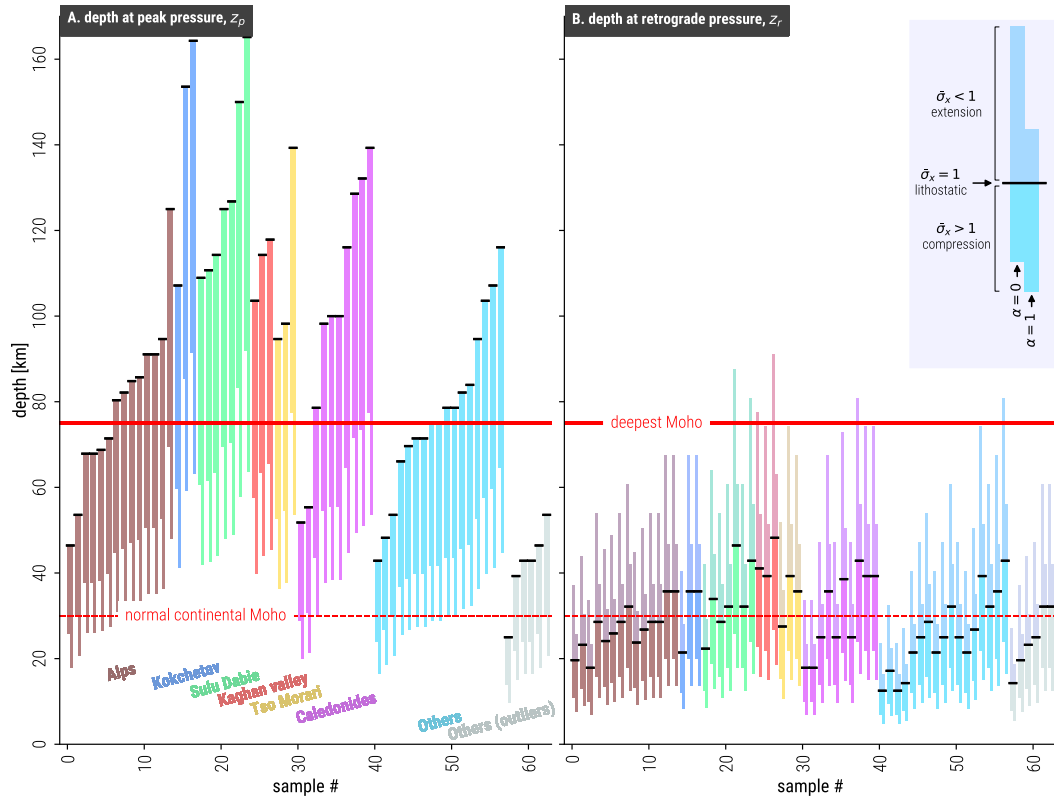


Figure 4. Depth estimates at peak pressure (A) and at retrograde pressure (B) for all samples in our dataset. Colors are coded for areas. The "normal Moho" depth corresponds to the average depth of the continental Moho in regions where the crust is neither thickened nor thinned and is 30 km. The deepest Moho (75 km) corresponds to the current depth of the Moho below the Tibetan Plateau. This figure can be reproduced using the computer script from supplementary information S4.

208 are shown only for compressive stress states (Fig. 4A), while depth estimates at retro-
 209 grade pressure (z_r) are shown for both compressive and extensional stress states (Fig.
 210 4B). We indicate two reference depths: (a) 30 km (red dashed line), which is the depth
 211 of a "normal continental Moho" defined as the thickness of an isostatically balanced con-
 212 tinental crust with topography at sea level, and (b) 75 km (thick red line), which is the
 213 depth of the Moho below the Tibetan Plateau and is the present-day "deepest Moho"
 214 on Earth. For each sample, the black horizontal bar indicates the lithostatic pressure case.
 215 The two columns for each sample indicate the two extreme deformation regimes: flat-
 216 tening ($\alpha = 0$, or $\sigma_2 = \sigma_3$) and constriction ($\alpha = 1$, or $\sigma_2 = \sigma_1$).

217 At peak pressure conditions, the upper estimate of depth z_p (Fig. 4A, black bars)
 218 corresponds to lithostatic conditions (i.e., with no deformation), with a conversion ra-
 219 tio $z/P = 35\text{km}/\text{GPa}$ (Fig. 4A and Fig. 3C). Under this condition, z_p values are ap-
 220 proximately 165 km for samples from the Kokchetav and Sulu-Dabie regions, 140 km for
 221 the Tso Morari and Caledonides, and 120 km for the Alps and Kaghan valley. The min-
 222 imum estimate of z_p results from assuming constricting deformation at brittle failure un-
 223 der compression (i.e., $\alpha = 1$ and $\bar{\sigma}_x = \Phi$). The conversion ratio is then $z/P = 16\text{km}/\text{GPa}$
 224 (Fig.3E) and $z_p < 75\text{km}$ for all samples, i.e., shallower than the present-day deepest
 225 Moho on Earth. The uncertainty range for z_p for a single data point varies from ≈ 15 km
 226 for sample #40 to ≈ 100 km for samples #16 and #23.

227 Under retrograde conditions, the lithostatic case represents an intermediate esti-
 228 mate because we consider both compressive and extensive tectonic regimes (Fig. 4B).
 229 The upper estimate for z_r results from assuming flattening deformation at brittle fail-
 230 ure in extension (i.e., $\alpha = 0$ and $\bar{\sigma}_x = 1/\Phi$). The conversion ratio is then $z/P = 64\text{km}/\text{GPa}$
 231 (Fig. 3A). A few samples from the Alps have a maximum depth estimate of $z_r > 85$
 232 km. For samples from the Kokchetav and Sulu-Dabie orogens, $z_r = 75$ km, and $z_r =$
 233 50 km for samples from the Kaghan valley, Tso Morari and Caledonides. The minimum
 234 estimate of z_r results from assuming constricting deformation at brittle failure in com-
 235 pression (i.e., $\alpha = 1$ and $\bar{\sigma}_x = \Phi$). z_r can be as shallow as 10 to 20 km for all sam-
 236 ples. The uncertainty range on the estimate of z_r for a single data point is up to 70 km
 237 for sample #11 whose maximum depth is ≈ 90 km. All samples have at least part of
 238 their range shallower than the deepest present-day Moho at both peak and retrograde
 239 pressures.

240 Figure 5A shows the estimated exhumation calculated as the difference between
 241 z_p and z_r . We present six special cases involving different values of $\bar{\sigma}_x^p$, $\bar{\sigma}_x^r$, α_r , and α_p
 242 to illustrate the dependence of the estimated exhumation on the stress state. In Figure
 243 5(C-H), we present Mohr diagrams for these six cases calculated using P_p and P_r from
 244 a reference sample.

245 The maximum exhumation is predicted when P_p corresponds to lithostatic pres-
 246 sure and P_r is recorded at brittle failure in compression (Fig. 5A, top of color bars, and
 247 Fig. 5C). The maximum predicted exhumation in our dataset varies between 20 and 150
 248 km.

249 We use the term "always lithostatic" for the case where both P_p and P_r are litho-
 250 static pressures. This case is shown with black horizontal bars in Figure 5A-B and il-
 251 lustrated in Figure 5D. In this case, exhumation varies between 25 km and 125 km for
 252 our dataset. Since the "always lithostatic" case is the most commonly used solution in
 253 the literature, we use it as a reference to normalize the results. The normalized graph
 254 (Fig. 5B) allows us to express the exhumation amount as a percentage of a reference case
 255 and outline similarities between samples.

256 The red rectangle symbol (Fig. 5A-B) corresponds to a case where deformation is
 257 compressive for P_p and extensive for P_r , the magnitude of deviatoric stress is a quarter
 258 of the maximum value, and deformation is plane strain (Fig. 5E). This stress state rep-

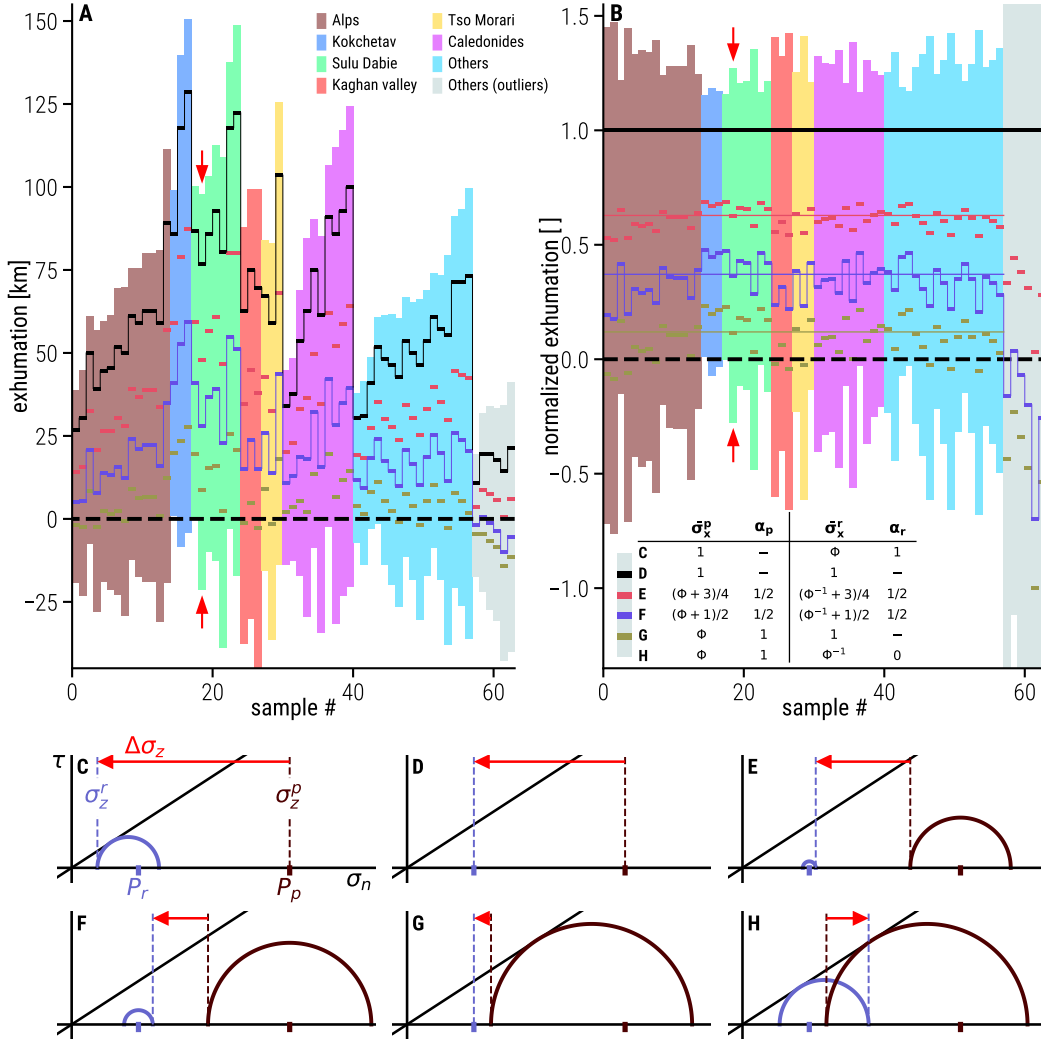


Figure 5. (A) Estimated amount of exhumation calculated as the difference between the estimated depth at peak and retrograde pressures ($z_p - z_r$) for all samples from our dataset. Bar colors indicate the provenance. (B) Same as (A) but normalized by the amount of exhumation obtained by considering P_p and P_r as lithostatic pressures (i.e., "always lithostatic" case). We calculated six special cases by combining different values of $\bar{\sigma}_x^p, \bar{\sigma}_x^r, \alpha_p, \alpha_r$, i.e., maximum and minimum exhumation, and four intermediate cases (colored rectangles). The values used are shown in the table inset in (B). (C-H) Mohr diagrams for the six special cases using P_p, P_r from a reference sample indicated by red arrows in (A) and (B). The characteristics of the special cases are (C) maximum exhumation case, (D) "always lithostatic" case, (E-F) cases with moderate deviatoric stress, (G) exhumation amount close to zero, and (H) minimum exhumation (negative exhumation, i.e., burial). This figure can be reproduced using the computer script from supplementary information S5.

259 represents a conservative estimate for rocks that deform by viscous deformation at depth.
 260 This low deviatoric stress has a significant impact on the quantity of exhumation: on av-
 261 erage, this case results in an estimate of exhumation that is only 60% of that for the "al-
 262 ways lithostatic" case (see red line in Fig. 5B). The blue rectangle symbol (Fig. 5A-B)
 263 represents a case of intermediate stress where the magnitude of deviatoric stress is half
 264 of the maximum value (Fig. 5F). On average, this case's results are 35% of the estimate
 265 for the "always lithostatic" case (see red line in Fig. 5B). The dark yellow rectangles indi-
 266 cate the scenario where deformation is brittle in compression at peak pressure, and P_r
 267 corresponds to lithostatic pressure under plane strain deformation. This scenario pre-
 268 dicted at most 30 km of exhumation and a minimum of -10 km (i.e., 10 km of additional
 269 burial). In this case, the predicted exhumation is $\approx 10\%$ of that for the "always litho-
 270 static" case, on average. The minimum exhumation estimate is obtained when deforma-
 271 tion is brittle and constrictive in compression for P_p , and deformation is brittle in ex-
 272 tension and occurs by flattening for P_r . The minimum exhumation estimate is between
 273 0 and -50 km.

274 For most samples, the normalized amount of exhumation for a specific case, e.g.,
 275 low stress (red rectangles), is contained within a small range around an average value.
 276 However, the samples from the category "Others (outliers)" have significantly different
 277 values. Although their values of P_p and P_r are not anomalous (e.g., Fig. 1), their com-
 278 bination clearly differs from other samples (see Fig. 1C). The relatively low dispersion
 279 of exhumation is related to the apparent proportionality between P_p and P_r (see Fig.
 280 1C).

281 In this section, we show that one can interpret the transition from P_p to P_r as the
 282 result of exhumation from great depth (Fig. ??C-D). The data are also compatible with
 283 an opposite interpretation: that this transition is the result of a change in stress state
 284 while depth is constant (Fig. ??G) or even while burial continues (Fig. ??H).

285 3 Two-point method of pressure-to-depth conversion

286 In this section, we re-examine our dataset with the additional constraint that $z_p =$
 287 z_r . In this way, we can use P_p and P_r together to reduce the uncertainty range for the
 288 depth estimate. We call this method "two-point pressure-to-depth conversion". In the
 289 case of a homogeneous rock and ignoring the possible role of fluids, the stress state can
 290 be modified in only two ways: (1) by modifying the magnitude of the horizontal stress
 291 or (2) by rotating the stress field. We explore these mechanisms independently, as well
 292 as a special case, in the following sections.

293 3.1 Mechanism 1: change in the magnitude of horizontal stress (S-model1)

294 First, we consider the change in pressure triggered by a change in the magnitude
 295 of the horizontal stress ($\bar{\sigma}_x$). Figure 6A shows five Mohr circles constructed with var-
 296 ious values of $\bar{\sigma}_x$. Note that the Mohr circle with $\bar{\sigma}_x = 1$ is a point. In Figure 6B-J,
 297 we represent our dataset as colored circles in the P_p vs. P_r space. These data points are
 298 placed on top of a colored contour map of $\bar{\sigma}_x^r$ computed for given values of $P_p, P_r, \bar{\sigma}_x^p, \alpha_p, \alpha_r$,
 299 where subscripts or superscripts p and r refer to the peak and retrograde stages, respec-
 300 tively. The values used are indicated at the top of columns and the beginning of rows
 301 of panels. A contour map of $z = z_p = z_r$ is also shown (black horizontal lines). The
 302 range of values calculated for $\bar{\sigma}_x^r$ covers stress states that do not exceed the Coulomb fail-
 303 ure criterion. Gray areas correspond to areas where $\bar{\sigma}_x^r$ has no meaningful solution (i.e.,
 304 because the stress magnitude would exceed the brittle yield stress). This means that the
 305 model cannot explain data plotting in the gray area. In contrast, when a data point is
 306 on top of the colored contour map, the combination of P_p, P_r for this data point can be
 307 obtained using eqs. 13 to 16, the combination of $\bar{\sigma}_x^p, \alpha_p, \alpha_r$ given and the value of $\bar{\sigma}_x^r$ and
 308 z shown by the contour map.

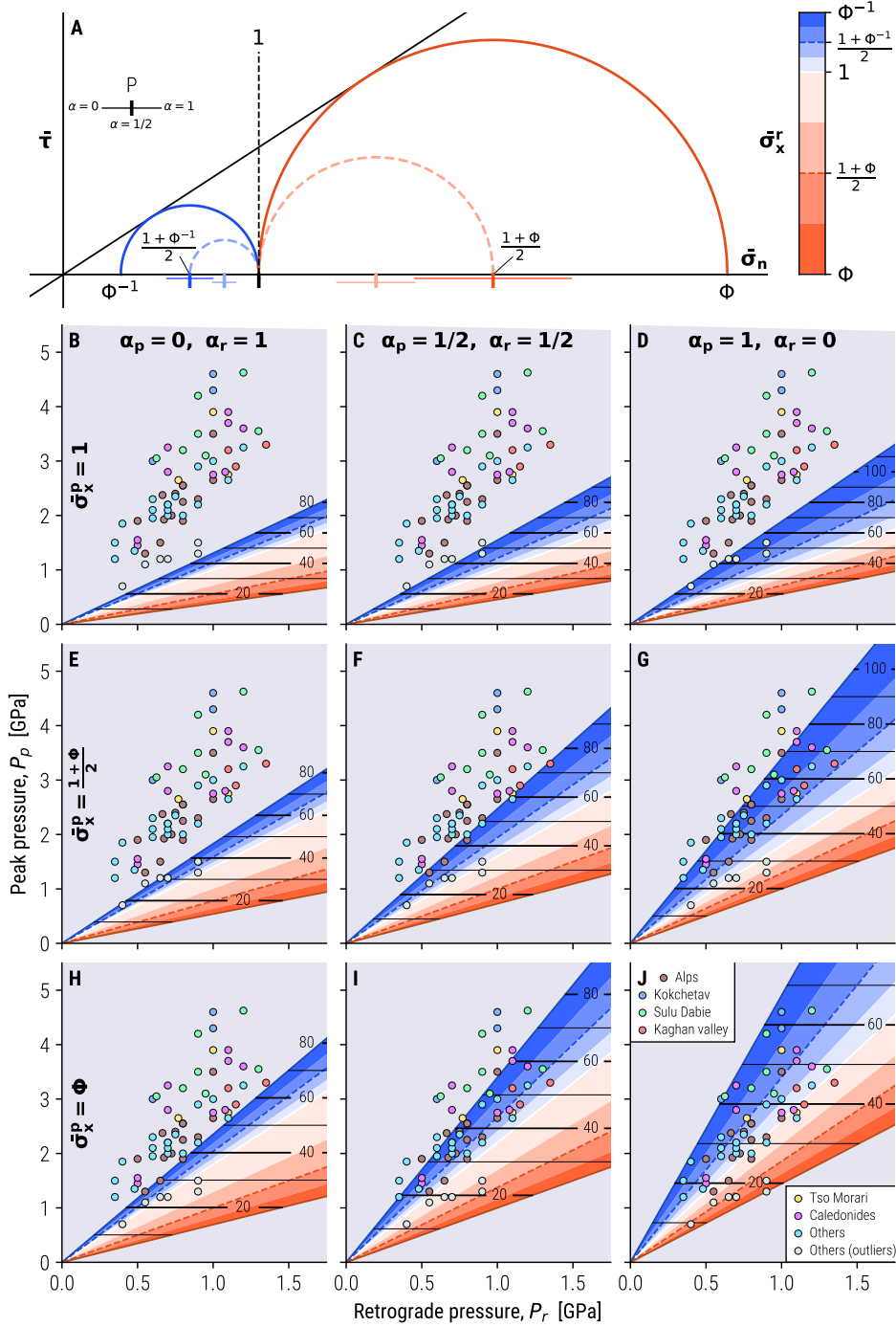


Figure 6. Results for the horizontal stress change-driven model. (J) A Mohr diagram illustrating the stress states associated with different values of $\bar{\sigma}_x$. The normal stress (horizontal axis) and shear stress (vertical axis) are normalized by σ_z . (B to J) Peak pressure as a function of retrograde pressure for data (colored circles) and model (colored contour plot). The estimated depths, in km, for each model are indicated by black contour lines. Gray areas indicate zones where the model does not have a solution (i.e., the deviatoric stress would exceed the yield stress). The model peak pressure is calculated from eq. (16) with parameters $\rho g = 28000 \text{ kg/m}^2/\text{s}$, $\tan(\phi) = 0.65$, $\bar{\sigma}_x = \bar{\sigma}_x^p$, $\alpha = \alpha^p$. The model retrograde pressure uses $\bar{\sigma}_x^r$, α^r . Each panel in a row uses the value of $\bar{\sigma}_x^p$ indicated in the leftmost panel of the row. Each panel in a column uses the values of α^p and α^r indicated at the top of the column. This figure can be reproduced using the computer script from supplementary information S6.

309 When the stress state is lithostatic at peak conditions, i.e., $\bar{\sigma}_x^p = 1$, only outliers
 310 plot in the solution domain (Fig. 6B to D), which means that the transition from P_p to
 311 P_r observed in the data cannot be explained only by increasing or decreasing the hor-
 312 izontal stress at constant depth if the stress state is lithostatic under peak conditions.
 313 When the initial horizontal stress is $\bar{\sigma}_x^p = (1 + \Phi)/2$, a few data points lie in the solu-
 314 tion domain for the combinations $\alpha_p = 0, \alpha_r = 1$ (Fig. 6E) and $\alpha_p = \alpha_r = 1/2$ (Fig.
 315 6F). However, approximately half of the points lie in the solution domain when $\alpha_p =$
 316 $1, \alpha_r = 0$ (Fig. 6G). Outliers can be explained by $\bar{\sigma}_x^r > 1$ (i.e., compressive stress state),
 317 while other points are explained by $\bar{\sigma}_x^r < 1$ (i.e., extensional stress state, Fig. 6G). When
 318 the initial horizontal stress is $\bar{\sigma}_x^p = \Phi$ (i.e., brittle deformation), few data points lie in
 319 the solution domain for the combinations $\alpha_p = 0, \alpha_r = 1$ (Fig. 6H). When $\alpha_p = \alpha_r =$
 320 $1/2$, half the points lie in the solution and these points correspond to values of $\bar{\sigma}_x^r < 1$
 321 (except for outliers, Fig. 6I). When $\alpha_p = 1, \alpha_r = 0$, all the points have a solution (Fig.
 322 6J). Most points have $\bar{\sigma}_x^r < 1$, but a few points are also associated with small values
 323 $\bar{\sigma}_x^r > 1$. Outliers are characterized by high values of $\bar{\sigma}_x^r$.

324 In all models except the one in Fig. 6J, some data points have a higher P_p than
 325 acceptable within the model bounds. On the other hand, there is no data point with P_p
 326 lower (or P_r higher) than that predicted by the model. The outlier points also plot within
 327 the bounds of the model. Overall, each data point is within the model boundaries or close
 328 to its boundary on at least one graph (e.g., Fig. 6J). Therefore, the model where the tran-
 329 sition from P_p to P_r is triggered by a change in the stress state at constant depth ($z_p =$
 330 z_r) explains the data. While some points lie within the model boundaries only for a de-
 331 viatoric stress with a large magnitude, other points can be explained by a change in stress
 332 with only moderate deviatoric stresses (Fig. 6G). Values of α_p, α_r are also important to
 333 explain the data; e.g., some data points can be explained only when $\alpha_p = 1, \alpha_r = 0$.
 334 For these data points, the model predicts a change in the mode of deformation from con-
 335 striction to flattening during the transition from P_p to P_r . Therefore, analyses of the mode
 336 of deformation in metamorphic rock samples provide a way to validate or falsify our model.

337 We compute the depth depending on the given value of $\bar{\sigma}_x^p$ and α_p from eqs. 14 and
 338 16. For $\bar{\sigma}_x \geq 1$, the pressure-to-depth conversion ratio increases with decreases in both
 339 $\bar{\sigma}_x$ and α (see Fig. 3). Graphically, this is expressed as the spacing between depth con-
 340 tours widening towards the right (e.g., from 6B to D) and bottom panels (e.g., from 6B
 341 to H). The cases where $\bar{\sigma}_x^p = 1$ provide the highest pressure-to-depth conversion, but
 342 only outliers lie within the solution domain. Their maximum depth is approximately 55
 343 km (Fig. 6D). The deepest depth estimates, approximately 75 km, are obtained when
 344 $\bar{\sigma}_x^p = (1 + \Phi)/2$ (Fig. 6F-G). In the case where $\bar{\sigma}_x^p = \Phi$, many points lie in the solu-
 345 tion range, but a low pressure-to-depth conversion ratio limits the depth. Thus, the max-
 346 imum depth is approximately 65 km (Fig. 6I-J). We discuss depth estimates in detail
 347 in section 3.4.

348 **3.2 Mechanism 2: stress rotation (S-model2)**

349 We now consider the change in pressure triggered by a rotation of the stress field.
 350 We assume that when the rock records P_p , the vertical and horizontal directions are prin-
 351 cipal stress directions, as in the previous sections. Then, the stress field rotates by an
 352 angle θ around axis y , and the rock records P_r . Figure 7A shows Mohr circles with five
 353 different values of θ .

354 Graphically, when we apply a rotation to a stress state where σ_1 is initially hor-
 355 izontal (i.e., compressional tectonic regime), the Mohr circle is shifted to the left (Fig.
 356 7A). The maximum shift corresponds to $\theta = 90^\circ$, and σ_1 is vertical (i.e., extensional
 357 tectonic regime). Eventually, the Mohr circle may become tangent to the Coulomb yield
 358 envelope. Since the model does not admit stress states beyond this envelope, the radius

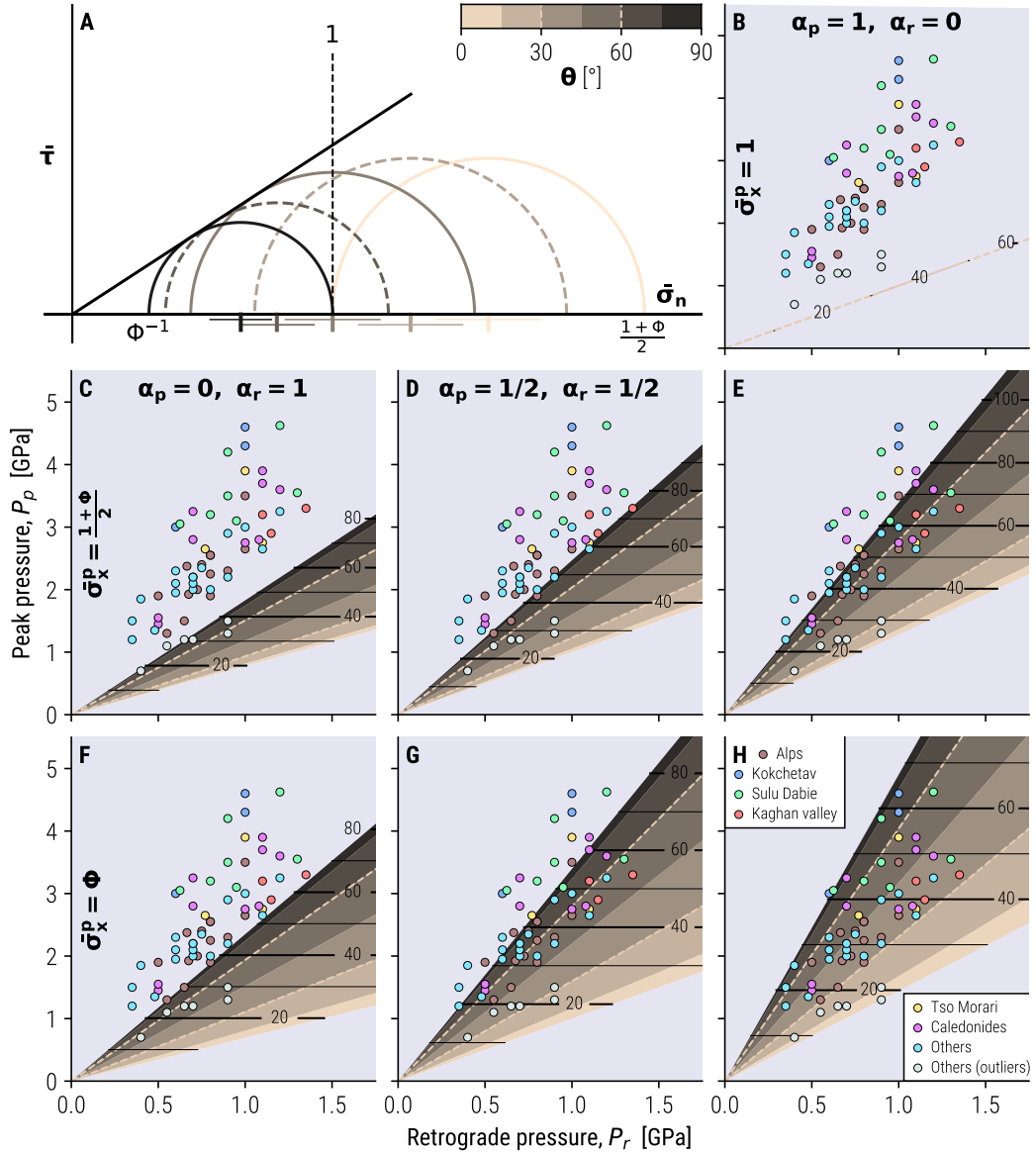


Figure 7. Summary of results for the stress rotation-driven model. θ is the counterclockwise rotation angle. (A) Mohr diagram illustrating the stress states associated with different amounts of rotation. The normal stress (horizontal axis) and shear stress (vertical axis) are normalized by σ_z . (B to H) Peak pressure as a function of retrograde pressure for different parameters (see text for details). Colored dots correspond to the data from our dataset. The estimated depths, in km, for each model are indicated by black horizontal lines. Gray areas indicate zones where the model does not have a solution. We use parameters $\rho g = 28000 \text{ kg/m}^2/\text{s}$ and $\tan(\phi) = 0.65$. Each panel in a row uses the value of $\bar{\sigma}_x^p$ indicated in the leftmost panel of the row. Each panel in a column uses the values of α^p and α^r indicated at the top of the column. The colors of the contour maps are coded for values of θ . This figure can be reproduced using the computer script from supplementary information S7.

359 of the Mohr circle has to decrease upon further rotation to remain tangent to it (see Fig.
360 7A, $\theta \geq 45^\circ$).

To formalize this behavior mathematically, we first define the yield function for Mohr-Coulomb plasticity:

$$F = \frac{\sigma_1 - \sigma_3}{2} - \frac{\sigma_1 + \sigma_3}{2} \sin \phi. \quad (18)$$

Then, the principal stresses σ_1 and σ_3 as a function of θ are expressed as

$$\text{when } F < 0, \begin{cases} \sigma_3 = \sigma_z \left(1 + (\bar{\sigma}_x^p - 1) \frac{\cos 2\theta - 1}{2} \right), \\ \sigma_1 = \sigma_z + \tau_{II}(\cos 2\theta + 1), \end{cases} \quad (19)$$

$$\text{when } F = 0, \begin{cases} \sigma_3 = \frac{2\sigma_z}{1 + \Phi - \frac{\Phi - 1}{\cos 2\theta}}, \\ \sigma_1 = \Phi \sigma_3. \end{cases} \quad (20)$$

361 Note that the first equation is only valid for $\bar{\sigma}_x^p \geq 1$. σ_2 is calculated using eq. 4, P_p
362 is the mean stress for $\theta = 0$, and P_r is the mean stress for a given value of θ .

363 Figures 7B-H are constructed in the same way as Figure 6, but the brownish col-
364 ored contour map now represents θ .

365 A lithostatic stress state is isotropic. Thus, pressure remains constant upon rota-
366 tion $\bar{\sigma}_x^p = \bar{\sigma}_x^r = P_p = P_r = 1$ (Fig. 7B). The resulting line in the P_p, P_r space does
367 not cross the data cloud, i.e., does not explain the data. For stress states tangent to the
368 Coulomb envelope, the upper limit of the contour map for θ ($\theta = 90^\circ$) is the same as
369 the upper limit of $\bar{\sigma}_x^r$ ($\bar{\sigma}_x^r = 1/\Phi$) (see Fig. 6), while the lower limit ($\theta = 0^\circ$) corre-
370 sponds to the case $\bar{\sigma}_x^r = \bar{\sigma}_x^p$ in the previous model. Therefore, the boundaries of the model
371 are similar for this model (involving θ) and for the previous model (involving $\bar{\sigma}_x^r$). Al-
372 though extreme stress states are identical, intermediate cases are different (e.g., compare
373 Figs. 6A and 7A). When $\bar{\sigma}_x^p = (1 + \Phi)/2$, a minimum of $\theta = 45^\circ$ is required to ex-
374 plain the data (Fig. 7C-E). As with the previous model, all data points are consistent
375 with a model where $\bar{\sigma}_x^p = \Phi, \alpha_p = 1, \alpha_r = 0$ (Fig. 7H). In this case, outliers are ex-
376 plained by $\theta = 0-30^\circ$ and other points by $\theta = 30-90^\circ$. Since the depth contour map
377 is computed based on $\bar{\sigma}_x^p, \alpha_p$ only and the model range is similar to the previous model,
378 the remarks concerning depth made in section 3.1 also apply here.

379 Since both this model (Fig. 6) and the previous one (Fig. 7) can explain the data,
380 there is an ambiguity about which mechanism is responsible for the stress change. Once
381 again, the predictions of this model can be validated or falsified using strain data. In-
382 deed, the rotation of the principal stress directions implies a rotation of the principal strain
383 direction.

384 3.3 A special case: compression to extension in the brittle limit (YB- 385 model)

386 When $\bar{\sigma}_x^p = \Phi$, depending on the values of α_p, α_r , the solution for $\theta = 90^\circ$ (which
387 corresponds to the upper limit of the solution domain) can outline the lower extent of
388 the data point cloud (Fig. 7F), pass through it (Fig. 7G), or outline its upper extent (Fig.
389 7H). In other terms, the data distribution can also be explained by a more restrictive
390 model where depth is constant, $\bar{\sigma}_x^p = \Phi, \theta = 90^\circ$ (or $\bar{\sigma}_x^r = 1/\Phi$, cf. Fig. 6) and α_p
391 and α_r are free parameters. This model has previously been employed by Yamato and
392 Brun (2017). Here, we extend their analysis by providing the associated pressure-to-depth
393 conversion.

To obtain a mathematical expression for P_p , we substitute eq. (14) with $\bar{\sigma}_x = \Phi$
for \bar{P} in eq. (16) and solve for P . For P_r , we use eq. (13) with $\bar{\sigma}_x = 1/\Phi$ instead of eq.

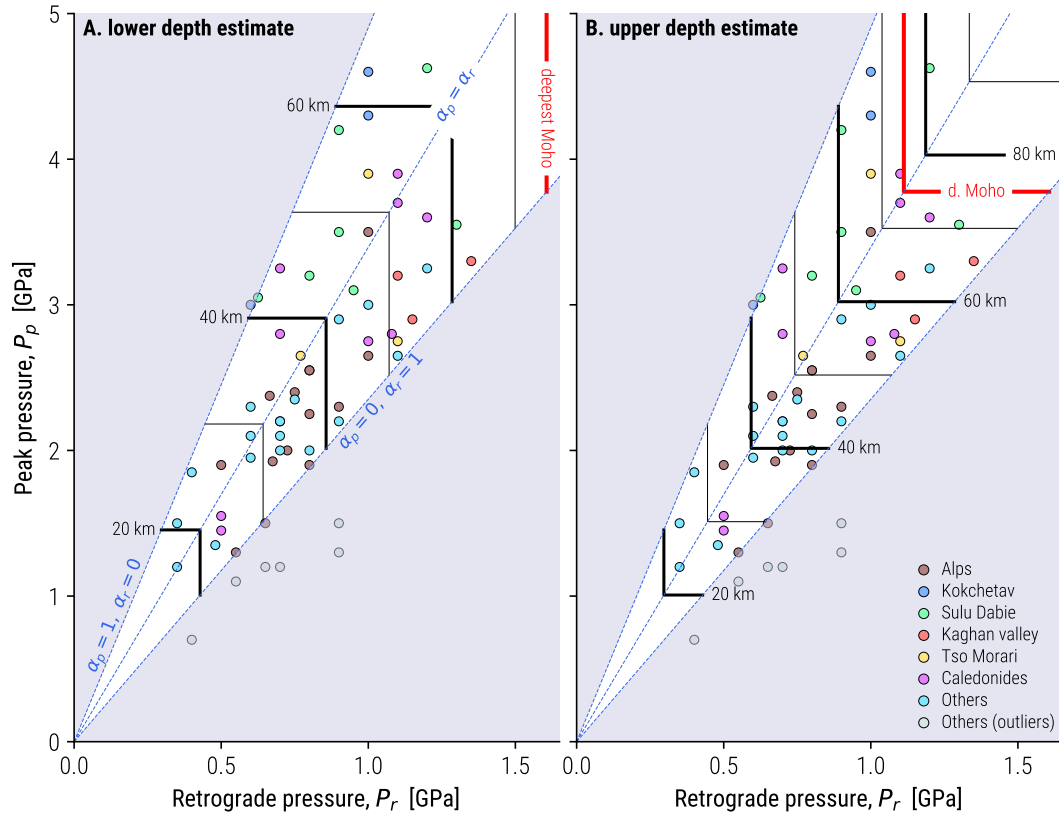


Figure 8. Data points in the P_p vs. P_r space. Contours of depth according to (a) the lower estimate and (b) upper estimate of our model. The model has solutions within the white fan and no solution in the gray domain. The color of the data points indicates the geographic region. This figure can be reproduced using the computer script from supplementary information S8.

(14). This process yields:

$$P_p = \frac{\rho g z}{3} (2 - \alpha^p + \Phi(1 + \alpha^p)), \quad (21)$$

$$P_r = \frac{\rho g z}{3} (1 + \alpha^r + \Phi^{-1}(2 - \alpha^r)). \quad (22)$$

394 Similar to previous figures, Figure 8 shows the domain of the solution of eqs. (21)
 395 and (22) for values of α_p and α_r between 0 and 1. Data points are also plotted in this
 396 P_p vs. P_r space. We also show contours of depth obtained by solving eq. (21) or (22)
 397 for z . The value of ρg influences the distance between depth contours but not the shape
 398 of the solution domain. The parameter Φ (or ϕ , cf eq. 11) controls the orientation and
 399 opening angle of the fan-shaped solution domain. The outlier points (gray) lie outside
 400 the solution domain, while the other data points (colored) lie within it or close to its bound-
 401 ary. The location of a point within the solution domain reflects the depth and mode of
 402 deformation under peak and retrograde conditions (α_p, α_r). Points along the central line
 403 $\alpha_p = \alpha_r$ have the same mode of deformation in the peak and retrograde stages. Points
 404 below this line deform by flattening under peak conditions and by constriction under ret-
 405 rograde conditions, and points lying above the central line deform by constriction un-
 406 der peak conditions and by flattening under retrograde conditions. Samples from one oro-
 407 gen tend to span a large range of α_p, α_r that could reflect local differences in the mode
 408 of deformation.

409 For a given depth, a range of P_p, P_r is possible depending on the value of α_r, α_p
 410 (see eqs. 21 and 22). The opposite is also true: for a given P_p, P_r , there is a range of pos-
 411 sible depths. We represent the lower and upper estimates of this range in Figures 8A and
 412 8B, respectively. In this model, all points lie below the "deepest Moho" reference depth
 413 for the lower depth estimate, and only one point is deeper than the "deepest Moho" when
 414 using the upper depth estimate.

415 3.4 Depth estimates using the two-point method

416 Figure 9 shows depth estimates for our data according to the horizontal stress change-
 417 driven model and the stress rotation model ("S-model", thin bars) and the compression
 418 to extension model of the previous section ("YB-model", thick bars). Depth estimates
 419 for peak pressure assuming a lithostatic stress state (see section 2.3) are also shown as
 420 the "L model" for reference (short bars).

421 In the following passage, we use the terms L-depth, S-depth and YB-depth to refer
 422 to the depth estimates according to the L-, S- and YB-models, respectively. The meth-
 423 ods for computing the depth ranges for the S-model and YB-model are given in Appendix
 424 A.

425 The minimum and maximum YB-depths are equal for points on the border of the
 426 solution domain fan, while the range is largest for points along the central line (Fig. 8).
 427 The range of S-depth tends to be larger for points with a low P_p/P_r ratio and decreases
 428 with increasing P_p/P_r (because fewer solutions exist; see Figs. 6 and 7). For all samples
 429 except the outliers, the S- and YB-depths are significantly lower than the L-depth. For
 430 example, one point in Kokchetav and one point in Sulu-Dabie have L-depths > 160 km,
 431 whereas their S- and YB-depths are 65–70 km and 60–85 km, respectively. For out-
 432 liers, the upper estimate of the S-depth is close to the L-depth. In the L-model, the depth
 433 is proportional to the peak pressure. Thus, large differences in peak pressure between
 434 two samples result in large differences in depth. However, the S- and YB-models take
 435 both peak and retrograde pressures into account, which can smooth out this difference.
 436 For example, the two data points with the highest pressures in the Alps have L-depths
 437 of 95 and 125 km, whereas the maximum S-depth is 70 km for both. Conversely, points
 438 with the same L-depth (i.e., same peak pressure) can have different YB- and S-depths.
 439 This contrast is best exemplified by comparing points with the same P_p in Figure 8: points

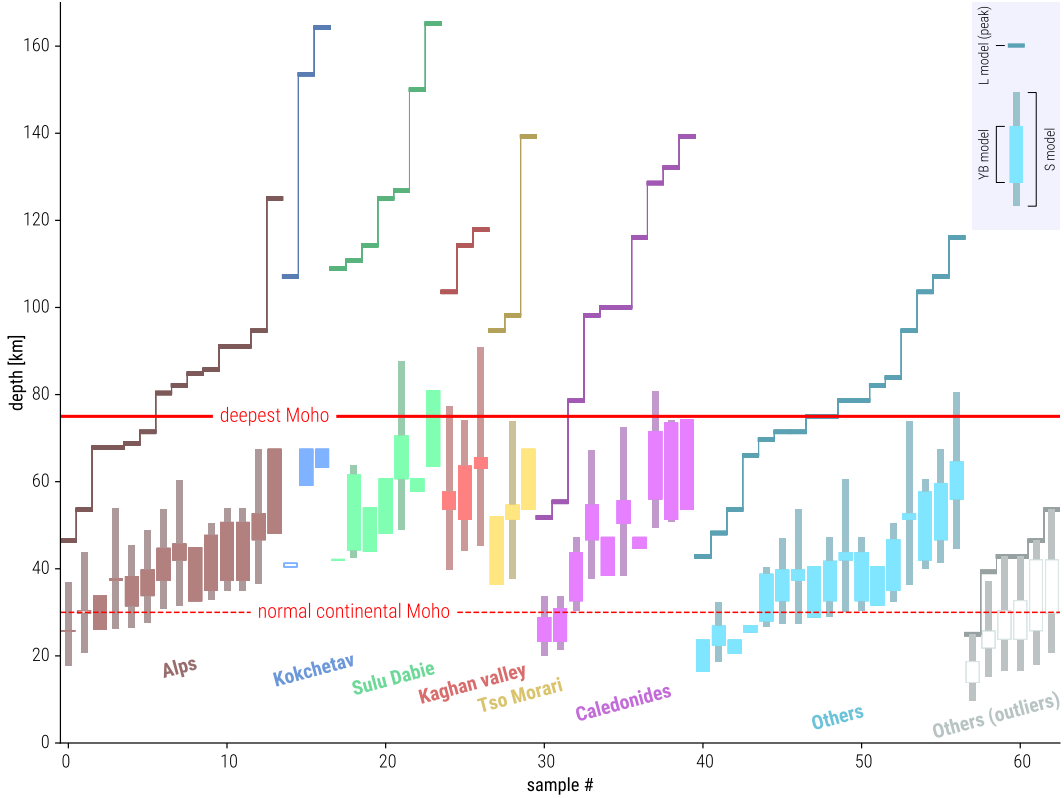


Figure 9. Estimated depth of each sample using the two-point method of pressure-to-depth conversion. The graph also shows depth estimates using the one-point lithostatic case for reference. L-model: peak pressure in the one-point lithostatic case. S-model refers to the models described in sections 3.1 and 3.2. The YB-model refers to the model described in section 3.3. For the YB-model, filled rectangles indicate depth estimates for points that lie within the model boundaries, while open rectangles apply to points outside the model boundaries. The depth estimates indicated by open rectangles are relevant for points close to the model boundary (e.g., samples #1 and #14) but less relevant for points far from the boundary (i.e., category Others (outliers)). This figure can be reproduced using the computer script from supplementary information S9.

440 in the upper half of the fan ($\alpha_p > \alpha_r$) align on a lower depth estimate contour, while
 441 points in the lower half of the fan ($\alpha_p < \alpha_r$) align on the upper depth estimate contour.
 442 Thus, at constant P_p , the mean depth estimate increases with increasing P_r , and
 443 the uncertainty increases towards the center of the fan ($\alpha_p = \alpha_r$ line). For example,
 444 for points at $P_p = 3GPa$, the mean depth estimate increases from 40 km at $P_r = 0.6GPa$
 445 to 60 km at $P_r = 1.2GPa$. At these two extreme P_r values, the depth estimate has a
 446 unique value, while at the center of the fan ($P_r = 0.85GPa$), the depth estimate ranges
 447 between 40 and 60 km. Overall, the most striking features of the S- and YB-models are
 448 that all data points have at least part of their range shallower than the "deepest Moho"
 449 line and that the deepest S-depth is approximately 90 km compared to 165 km for the
 450 L-depth.

4 Discussion

Pressure is a function of both depth and deviatoric stresses. However, since deviatoric stress cannot be measured, pressure-to-depth conversions require assumptions. In the previous sections, we propose several pressure-to-depth conversion methods involving one or two pressure data points. In particular, we show that the proportionality between P_p and P_r can be explained by a model where P_p and P_r are recorded by the rock at the same depth but under different stress states (Figs. 6 to 8). For simplicity, we only present two-point models with either stress rotation or horizontal stress magnitude change and no exhumation. Combining rotation and magnitude change may further decrease the magnitude of deviatoric stresses required to explain the data. Relaxing the assumption that $z_p = z_r$ and accounting for some exhumation would also decrease the magnitude of deviatoric stresses required.

4.1 Perspectives on using strain data

In our formulation of the pressure-to-depth conversion, we use α instead of a stress value (see eq. 4). α characterizes the shape of the stress ellipsoid and is thus similar to commonly used parameters for characterizing the shape of ellipsoid such as Lode's ratio or Flinn's k-value (Mookerjee & Peek, 2014). Because strain results from applied stress, obtaining a value for α using markers of deformation could provide key data to better constrain depth. The two-point models relying on a change in the magnitude of horizontal stress (Fig. 6) or stress orientation (Fig. 7) give ambiguous results since both models can explain the data. However, one could falsify the predictions of the model based on stress rotation (Fig. 7) by using the directions of the strain ellipsoid or paleostress inversion of fault orientations to estimate stress directions.

4.2 Data distribution and model

The data suggest that P_p and P_r are proportional (see Fig. 1). However, by using the one-point method, because P_p and P_r are considered independently, it is difficult to explain this proportionality. In the lithostatic case, for instance, the decompression from P_p to P_r is controlled only by the exhumation of rocks. However, the currently proposed exhumation mechanisms (e.g., subduction channels and corner flows) do not suggest that exhumation would be proportional to maximum depth. On the other hand, the two-point model treats both P_p and P_r together. Since we assume that $z_p = z_r$, the maximum change from P_p to P_r is limited by Byerlee's law, and the yield stress function is linearly dependent on P . Considering reasonable values for the friction coefficient (e.g., 0.65), the limits of the model outline the distribution of the data. For example, for the models shown in Figures 6J and 7H, the extent of the model domain outlines the upper extent of the distribution, and the lower limit of the model corresponds to the lower extent for outliers.

The YB-model simulates the case where rocks are brittle in both compression and extension and thus constitutes a particular case of the two-point model. It is interesting to note that although the YB-model allows us to largely explain the data, it excludes the outliers (Fig. 8). However, all data (including outliers) can be explained considering the more general S-models (Figs. 6 and 7).

The upper extent of the data distribution (P_p/P_r 4.8) can only be explained when $\bar{\sigma}_x^p = \Phi$, $\alpha_p = 1$ (brittle constrictive deformation in compression) and $\bar{\sigma}_x^r = 1/\Phi$, $\alpha_r = 0$ (brittle flattening deformation in extension). The lower extent of the data distribution excluding outliers (P_p/P_r 2.4), however, can have several explanations. In the YB-model, it corresponds to $\alpha_p = 0$, $\alpha_r = 1$. For S-models (e.g., Figs. 6G, I, J; 7E, G, H), the lower bound of the data can be within the solution domain and coincides with different values of $\bar{\sigma}_x^r$ or θ . Interestingly, the lower limit coincides with $S_{xr}=1$ (i.e., lithostatic case)

in Fig. 6J. Two-point models can fit all data points from the dataset (or lie very close to the model boundary), which suggests that in all orogens, a change in stress state may be responsible for the decompression from P_p to P_r . The different predictions in terms of the change mode of deformation (α_p to α_r) bring additional constraints concerning the mechanism responsible for the change in the stress state. Monitoring the evolution of α in 3D numerical geodynamic models may provide more answers.

4.3 Inclusion-host system

The models presented here explain pressure variations in a homogeneous material subjected to a change in depth or deviatoric stresses. In a heterogeneous system, the pressure in one material may be affected by deviatoric stresses in another material. A well-studied example is the case of an elliptical inclusion embedded in an elastic or linear viscous matrix. In this system, the magnitude and sense of deviatoric stresses are functions of the relative strength between the matrix and the inclusion, as well as the orientation of the inclusion in the stress field (D. W. Schmid & Podladchikov, 2003, 2005; Moulas et al., 2014). The pressure in the inclusion is controlled both by the stress state in the inclusion and by the stress state in the host rock. An important point is that deviatoric stresses in a weak inclusion may be negligible, while the pressure can still be as high as $\sigma_1 = \Phi$ in a strong host rock. This is very different from a homogeneous material where the pressure is lithostatic in the absence of deviatoric stresses. Thus, pressure can vary between the values of σ_3 and σ_1 for the strongest material in the inclusion/host system, whereas in a homogeneous material, pressure can vary only between $2/3\sigma_3+1/3\sigma_1$ and $1/3\sigma_3+2/3\sigma_1$ (see eq. (6)) (Moulas et al., 2014; Schmalholz & Podladchikov, 2013). Field examples of this phenomenon have been documented by Luisier et al. (2019) in the Monte Rosa nappe (Alps) and by Jamtveit et al. (2018) in the Bergen Arc (Caledonides).

4.4 Local vs. regional stress state

In this paper, we present several methods that can be used to determine possible stress states associated with peak and metamorphic pressures. Stress states are by essence local. Some researchers even propose that metamorphic pressure may reflect the stress state in only a single grain (see the discussion about inclusions in the previous paragraph) and that large pressure gradients responsible for pressure differences on the order of GPa can be recorded within a single grain (Tajčmanová et al., 2014, 2015). In our dataset, samples from the same region have a wide variety of P_p/P_r ratios (see Fig. 1C) and are often distributed from one side of the fan to another (between $P_p/P_r = 1.4$ and $P_p/P_r = 4.8$), which indicates differences in the change in stress magnitude, stress orientation or relative magnitude of σ_2 (α). This could be an indication that pressure data reflect the local (grain- to 10 km-scale) rather than regional (100 km) stress state. Thus, using the stress states determined in this study to interpret regional-scale processes requires taking some caution. For example, the YB-model assumes that the peak to retrograde pressure can be explained by a transition from a compressional to an extensional stress state, with both stress states close to the brittle limit. These stress states reflect km-scale conditions or are smaller in the sense that the whole system is submitted to convergence (i.e., in Fig. 1). The distance between two points far from the subduction zone, one located on the subducting plate and the other located on the overriding plate, is constantly decreasing, but the part undergoing exhumation is locally subjected to extension. This corresponds well with the fact that the exhumation of a coherent metamorphic unit is impossible without a normal fault on top. As we have shown, stress orientation has a strong control on pressure changes, and in a complex orogen, stress orientations can vary significantly in space and time, e.g., due to changes in the subduction angle or the friction along the plate boundary (Wang & Hu, 2006), the proximity to magma chambers (Gerbault et al., 2018) or faults (e.g., Shao & Hou, 2019; Martínez-Díaz, 2002; Maerten et al., 2002), or the position within the orogen (e.g., Kastrup et al., 2004).

4.5 Implications for geodynamic models

Rock strength strongly depends on temperature. Hence, considering classic rheological yield stress envelopes (e.g., E. B. Burov, 2011), it seems inadequate to consider large deviatoric stresses deep in the lithosphere (> 120 km) due to the temperature increase with depth. This statement could favor using lithostatic pressure-to-depth conversion but remains debatable. Indeed, the depth estimates using the S- and YB-models are consistent with the depth of the crustal roots of orogens, and in these places (i.e., at the base of the crust or in the lithospheric mantle), significant deviatoric stresses are possible. Significant deviatoric stresses are even more likely at this depth in a subduction zone with a cold geotherm.

Several elements suggest significant deviatoric stresses near the Moho depth: (1) earthquakes are not uncommon at such depths in a subduction context and provide evidence that brittle deformation can occur (e.g., B. Hacker et al., 2003; Hetényi et al., 2007), and (2) several field and petrological studies have already evidenced brittle deformation associated with HP metamorphism (e.g., Austrheim & Boundy, 1994; John & Schenk, 2006; Angiboust et al., 2012; Hertgen et al., 2017; Yang et al., 2014).

Samples with high P_p/P_r require a stress field close to the brittle limit using the S-model (e.g., Fig. 7). However, samples with $P_p/P_r < \Phi$ are consistent with a stress state where the magnitude of the deviatoric stress (second invariant) is only half that required for brittle deformation (i.e., $\bar{\sigma}_x^p = (1 + \Phi)/2$) when peak pressure is recorded. This means that even in the ductile realm, the effect of the deviatoric stresses should not be neglected.

The release of fluids from dewatering metamorphic reactions can decrease the effective pressure. Thus, one might argue that the transition from P_p to P_r is caused by fluid pressure. However, this mechanism seems unlikely because fluid pressure would need to remain high during exhumation (otherwise, a new peak pressure would be recorded). Townend and Zoback (2000) argue that high fluid pressure leads to rock fracturing, which creates space and thus causes fluid pressure to decrease.

5 Conclusion

In this contribution, we reviewed the basic mathematical formulations of pressure-to-depth conversion for a homogeneous rock. First, we derived the standard "one-point method of pressure-to-depth conversion" and applied it to a large dataset of metamorphic pressures to independently estimate a range of depths at which rocks may have recorded their peak (P_p) and retrograde pressures (P_r). Since the most common assumption in the literature is to consider that metamorphic pressure corresponds to the lithostatic pressure, we used this "lithostatic case" as a reference.

By introducing deviatoric stress components and considering only the compressional stress regime (σ_1 horizontal) at P_p and both compressional and extensional (σ_1 vertical) stress regimes for P_r , we showed that the deviations from the reference case can be significant. For P_p , the estimated depths vary between 40 and 100 % of the reference case. For P_r , the estimated depth range is 40–185% of the reference case. Thus, under our assumption, the lithostatic case represents an upper bound estimate of depth for P_p and an intermediate value for P_r . Moreover, the uncertainty ranges of both peak (z_p) and retrograde (z_r) depths are large enough to lead to overlap for these two depth estimates. This means that the transition from P_p to P_r can be triggered by exhumation, a change in the stress state at constant depth, or a combination of both processes.

Second, we presented "two-point methods of pressure-to-depth conversion" that use both P_p and P_r to estimate depth under the hypothesis that $z_p = z_r$. For the two-point method, we considered two mechanisms of stress change between P_p and P_r : (1)

600 change in the magnitude of horizontal stresses and (2) rotation of the stress state. We
 601 also treated a particular case where the magnitude of deviatoric stresses is maximum,
 602 and the stress regime varies from compression at P_p to extension at P_r . The two-point
 603 method greatly decreases the uncertainty range of depth estimates and yields stricter
 604 constraints on the possible stress state. Remarkably, all P_p, P_r points in our dataset are
 605 consistent with a change in the stress state at a constant depth.

606 In our dataset, the maximum depth estimates under the "lithostatic assumption"
 607 are approximately 160 km for P_p and 50 km for P_r . Thus, the lithostatic assumption re-
 608 quires deep burial and exhumation from great depth. On the other hand, the two-point
 609 models reveal that points in our dataset are consistent with depths shallower than 75
 610 km (i.e., the current deepest Moho). This suggests instead that all metamorphic rocks
 611 in our dataset have been buried at crustal depths with no (or only minor) exhumation
 612 between P_p and P_r . The validity of either of these models cannot be assessed based only
 613 on pressure and temperature data. However, the principal stress directions and the re-
 614 lative magnitude of σ_2 (i.e., α) may be estimated from the strain ellipsoid or paleostress
 615 analysis. Thus, a precise analysis of the deformation in association with the P estimates
 616 in metamorphic rocks could validate or falsify depth estimates from the two-point model
 617 and further decrease the depth estimate uncertainty.

618 Appendix A Depth estimates for the two-point model

619 A1 S-model

The depth estimate range for S-models is calculated numerically by testing a large
 array of combinations of $\bar{\sigma}_x^p$, α_p and α_r for each sample. The ranges considered are $1 \leq$
 $\bar{\sigma}_x^p \leq \Phi$ and $0 \leq \alpha_p, \alpha_r \leq 1$, and we use 50 values to discretize the range of each pa-
 rameter for a total of $50^3 = 125,000$ parameter combinations. We proceed in two steps.
 First, we compute σ_z using eq. (15) with $P = P_p$, $\bar{\sigma}_x = \bar{\sigma}_x^p$, and $\alpha = \alpha_p$, and we com-
 pute $z = \sigma_z / \rho g$. Second, we need to test whether the previous solution is within the
 acceptable bounds of the model (i.e., not in the gray area of Figs. 6 to 8). For this pur-
 pose, we compute $\bar{\sigma}_x^r$ using the following equation:

$$\begin{cases} \bar{\sigma}_x = \frac{3P/\sigma_z - 2 + \alpha}{1 + \alpha}, & \text{when } \bar{\sigma}_x \leq 0, \\ \bar{\sigma}_x = \frac{3P/\sigma_z - 1 - \alpha}{2 - \alpha}, & \text{when } \bar{\sigma}_x \geq 0, \end{cases} \quad (\text{A1})$$

620 with $P = P_r$, $\bar{\sigma}_x = \bar{\sigma}_x^r$, and $\alpha = \alpha_r$. Then, we test whether $1/\Phi \leq \bar{\sigma}_x^r \leq \Phi$ and up-
 621 date the range of depth if the test is successful.

622 A2 YB-model

623 To compute the range of depth for the YB-model, we use the minimum and up-
 624 per estimates of depth whose contours are plotted in Figures 8A and 8B, respectively.
 625 In practice, we compute σ_z using eq. (15) with parameters $[P, \alpha, \bar{\sigma}_x]$. For data points
 626 where $P_p/P_r > \Phi$ (i.e., above the line marked $\alpha_p = \alpha_r$ in Fig. 8), we use parameters
 627 $[P_p, 1, \Phi]$ to compute $\min(\sigma_z)$, and $[P_r, 0, 1/\Phi]$ for $\max(\sigma_z)$. For data points where $P_p/P_r \leq$
 628 Φ , we use $[P_r, 1, 1/\Phi]$ for $\min(\sigma_z)$ and $[P_p, 0, \Phi]$ for $\max(\sigma_z)$. Then, we compute $z =$
 629 $\sigma_z / \rho g$. In this algorithm, depth is calculated using either $[P_p, \alpha_p, \bar{\sigma}_x^p]$ or $[P_r, \alpha_r, \bar{\sigma}_x^r]$. If
 630 α_p is used as input, α_r can be computed back from σ_z , and we can perform the test $0 \leq$
 631 $\alpha_r \leq 1$ to verify that the solution is within the bounds of the model. If α_r is used as
 632 input, α_p is computed instead. If the test is successful, we plot the range as a colored
 633 box in Figure 9 or as an open box otherwise.

Acknowledgments

The database and computer code (Jupyter notebooks) allowing the reproduction of most figures are available as supplementary information and will be made available in a public repository once the paper is accepted for publication. This work was supported by the Japanese Society for the Promotion of Science (JSPS), Grant-in-Aid for Scientific Research no. JP18K13643.

References

- Agard, P., Yamato, P., Jolivet, L., & Burov, E. (2009, jan). *Exhumation of oceanic blueschists and eclogites in subduction zones: Timing and mechanisms* (Vol. 92) (No. 1-2). Elsevier. doi: 10.1016/j.earscirev.2008.11.002
- Anderson, E. M. (1905, jan). The dynamics of faulting. *Transactions of the Edinburgh Geological Society*, 8(3), 387–402. doi: 10.1144/transed.8.3.387
- Angiboust, S., Agard, P., Yamato, P., & Raimbourg, H. (2012, aug). Eclogite breccias in a subducted ophiolite: A record of intermediatedepth earthquakes? *Geology*, 40(8), 707–710. doi: 10.1130/G32925.1
- Austrheim, H., & Boundy, T. M. (1994). Pseudotachylytes generated during seismic faulting and eclogitization of the deep crust. *Science*, 265(5168), 82–83. doi: 10.1126/science.265.5168.82
- Beaumont, C., Jamieson, R. A., Butler, J. P., & Warren, C. J. (2009, sep). Crustal structure: A key constraint on the mechanism of ultra-high-pressure rock exhumation. *Earth and Planetary Science Letters*, 287(1-2), 116–129. doi: 10.1016/j.epsl.2009.08.001
- Beltrando, M., Hermann, J., Lister, G., & Compagnoni, R. (2007, apr). On the evolution of orogens: Pressure cycles and deformation mode switches. *Earth and Planetary Science Letters*, 256(3-4), 372–388. doi: 10.1016/j.epsl.2007.01.022
- Brace, W. F., Ernst, W. G., & Kallberg, R. W. (1970, may). An Experimental Study of Tectonic Overpressure in Franciscan Rocks. *GSA Bulletin*, 81(5), 1325–1338. doi: 10.1130/0016-7606(1970)81[1325:aesoto]2.0.co;2
- Brun, J. P., & Faccenna, C. (2008, jul). Exhumation of high-pressure rocks driven by slab rollback. *Earth and Planetary Science Letters*, 272(1-2), 1–7. doi: 10.1016/j.epsl.2008.02.038
- Burov, E., Francois, T., Yamato, P., & Wolf, S. (2014, mar). Mechanisms of continental subduction and exhumation of HP and UHP rocks. *Gondwana Research*, 25(2), 464–493. doi: 10.1016/j.gr.2012.09.010
- Burov, E. B. (2011, aug). Rheology and strength of the lithosphere. *Marine and Petroleum Geology*, 28(8), 1402–1443. doi: 10.1016/j.marpetgeo.2011.05.008
- Butler, J. P., Beaumont, C., & Jamieson, R. A. (2013, sep). The Alps 1: A working geodynamic model for burial and exhumation of (ultra)high-pressure rocks in Alpine-type orogens. *Earth and Planetary Science Letters*, 377-378, 114–131. doi: 10.1016/j.epsl.2013.06.039
- Butler, J. P., Beaumont, C., & Jamieson, R. A. (2014, jul). The Alps 2: Controls on crustal subduction and (ultra)high-pressure rock exhumation in Alpine-type orogens. *Journal of Geophysical Research: Solid Earth*, 119(7), 5987–6022. Retrieved from <http://doi.wiley.com/10.1002/2013JB010799> doi: 10.1002/2013JB010799
- Byerlee, J. (1978, jul). Friction of rocks. *Pure and Applied Geophysics PAGEOPH*, 116(4-5), 615–626. doi: 10.1007/BF00876528
- Chopin, C. (2003, jul). Ultrahigh-pressure metamorphism: Tracing continental crust into the mantle. *Earth and Planetary Science Letters*, 212(1-2), 1–14. doi: 10.1016/S0012-821X(03)00261-9
- Ernst, W. G. (1963). Significance Of Phengitic Micas From Low-Grade Schists — American Mineralogist — GeoScienceWorld. *American Mineralogist*, 48(11-

- 686 12), 1357–1373. Retrieved from [https://pubs.geoscienceworld.org/msa/](https://pubs.geoscienceworld.org/msa/amin/article-abstract/48/11-12/1357/542168)
687 [amin/article-abstract/48/11-12/1357/542168](https://pubs.geoscienceworld.org/msa/amin/article-abstract/48/11-12/1357/542168)
- 688 Ernst, W. G., Hacker, B. R., & Liou, J. G. (2007). Petrotectonics of ultrahigh-
689 pressure crustal and upper-mantle rocks—Implications for Phanerozoic colli-
690 sional orogens. *Geol. Soc. Am.*, *433*, 27–49.
- 691 Froitzheim, N., Pleuger, J., Roller, S., & Nagel, T. (2003, oct). Exhumation of high-
692 and ultrahigh-pressure metamorphic rocks by slab extraction. *Geology*, *31*(10),
693 925–928. doi: 10.1130/G19748.1
- 694 Gerbault, M., Hassani, R., Novoa Lizama, C., & Souche, A. (2018, mar). Three-
695 Dimensional Failure Patterns Around an Inflating Magmatic Chamber. *Geo-*
696 *chemistry, Geophysics, Geosystems*, *19*(3), 749–771. Retrieved from [http://](http://doi.wiley.com/10.1002/2017GC007174)
697 doi.wiley.com/10.1002/2017GC007174 doi: 10.1002/2017GC007174
- 698 Gerya, T. (2015, oct). Tectonic overpressure and underpressure in lithospheric tec-
699 tonics and metamorphism. *Journal of Metamorphic Geology*, *33*(8), 785–800.
700 Retrieved from <http://doi.wiley.com/10.1111/jmg.12144> doi: 10.1111/
701 [jmg.12144](http://doi.wiley.com/10.1111/jmg.12144)
- 702 Godard, G. (2001, aug). Eclogites and their geodynamics interpretation: A history.
703 *Journal of Geodynamics*, *32*(1-2), 165–203. doi: 10.1016/S0264-3707(01)00020-
704 5
- 705 Green, H. W. (2005). Psychology of a changing paradigm: 40+ Years of high-
706 pressure metamorphism. *International Geology Review*, *47*(5), 439–456. doi:
707 [10.2747/0020-6814.47.5.439](https://doi.org/10.2747/0020-6814.47.5.439)
- 708 Guillot, S., Hattori, K., Agard, P., Schwartz, S., & Vidal, O. (2009). Exhumation
709 Processes in Oceanic and Continental Subduction Contexts: A Review. In *Sub-*
710 *duction zone geodynamics* (pp. 175–205). Springer Berlin Heidelberg. doi: 10
711 [.1007/978-3-540-87974-9_10](https://doi.org/10.1007/978-3-540-87974-9_10)
- 712 Hacker, B., Peacock, S., Abers, G., & Holloway, S. (2003). Subduction factory 2.
713 Are intermediate-depth earthquakes in subducting slabs linked to metamorphic
714 dehydration reactions? *J. Geophys. Res.*, *108*, 2030.
- 715 Hacker, B. R., & Gerya, T. V. (2013, sep). *Paradigms, new and old, for ultrahigh-*
716 *pressure tectonism* (Vol. 603). doi: 10.1016/j.tecto.2013.05.026
- 717 Hertgen, S., Yamato, P., Morales, L. F., & Angiboust, S. (2017, jun). Evidence
718 for brittle deformation events at eclogite-facies P-T conditions (example of
719 the Mt. Emilius klippe, Western Alps). *Tectonophysics*, *706-707*, 1–13. doi:
720 [10.1016/j.tecto.2017.03.028](https://doi.org/10.1016/j.tecto.2017.03.028)
- 721 Hetényi, G., Cattin, R., Brunet, F., Bollinger, L., Vergne, J., Nábělek, J. L., & Di-
722 ament, M. (2007, dec). Density distribution of the India plate beneath the
723 Tibetan plateau: Geophysical and petrological constraints on the kinetics of
724 lower-crustal eclogitization. *Earth and Planetary Science Letters*, *264*(1-2),
725 226–244. doi: 10.1016/j.epsl.2007.09.036
- 726 Hobbs, B., & Ord, A. (2015, nov). *Dramatic effects of stress on metamorphic reac-*
727 *tions: COMMENT* (Vol. 43) (No. 11). Geological Society of America. doi: 10
728 [.1130/G37070C.1](https://doi.org/10.1130/G37070C.1)
- 729 Hobbs, B. E., & Ord, A. (2017, dec). Pressure and equilibrium in deforming rocks.
730 *Journal of Metamorphic Geology*, *35*(9), 967–982. Retrieved from [http://doi](http://doi.wiley.com/10.1111/jmg.12263)
731 [.wiley.com/10.1111/jmg.12263](http://doi.wiley.com/10.1111/jmg.12263) doi: 10.1111/jmg.12263
- 732 Huw Davies, J., & von Blanckenburg, F. (1995, jan). Slab breakoff: A model of
733 lithosphere detachment and its test in the magmatism and deformation of col-
734 lisional orogens. *Earth and Planetary Science Letters*, *129*(1-4), 85–102. doi:
735 [10.1016/0012-821X\(94\)00237-S](https://doi.org/10.1016/0012-821X(94)00237-S)
- 736 Jamieson, J. C. (1963, aug). Possible occurrence of exceedingly high pres-
737 sures in geological processes. *GSA Bulletin*, *74*(8), 1067–1070. doi:
738 [10.1130/0016-7606\(1963\)74\[1067:poehp\]2.0.co;2](https://doi.org/10.1130/0016-7606(1963)74[1067:poehp]2.0.co;2)
- 739 Jamtveit, B., Moulas, E., Andersen, T. B., Austrheim, H., Corfu, F., Petley-Ragan,
740 A., & Schmalholz, S. M. (2018, dec). High Pressure Metamorphism Caused by

- 741 Fluid Induced Weakening of Deep Continental Crust. *Scientific Reports*, 8(1),
742 1–8. doi: 10.1038/s41598-018-35200-1
- 743 John, T., & Schenk, V. (2006, jul). Interrelations between intermediate-depth
744 earthquakes and fluid flow within subducting oceanic plates: Constraints
745 from eclogite facies pseudotachylytes. *Geology*, 34(7), 557–560. doi:
746 10.1130/G22411.1
- 747 Kastrup, U., Zoback, M. L., Deichmann, N., Evans, K. F., Giardini, D., & Michael,
748 A. J. (2004, jan). Stress field variations in the Swiss Alps and the northern
749 Alpine foreland derived from inversion of fault plane solutions. *Journal of*
750 *Geophysical Research: Solid Earth*, 109(B1). doi: 10.1029/2003jb002550
- 751 Luisier, C., Baumgartner, L., Schmalholz, S. M., Siron, G., & Vennemann, T. (2019,
752 dec). Metamorphic pressure variation in a coherent Alpine nappe challenges
753 lithostatic pressure paradigm. *Nature Communications*, 10(1), 1–11. doi:
754 10.1038/s41467-019-12727-z
- 755 Maerten, L., Gillespie, P., & Pollard, D. D. (2002, jan). Effects of local stress pertur-
756 bation on secondary fault development. *Journal of Structural Geology*, 24(1),
757 145–153. doi: 10.1016/S0191-8141(01)00054-2
- 758 Mancktelow, N. S. (1993, nov). Tectonic overpressure in competent mafic layers and
759 the development of isolated eclogites. *Journal of Metamorphic Geology*, 11(6),
760 801–812. Retrieved from [http://doi.wiley.com/10.1111/j.1525-1314.1993](http://doi.wiley.com/10.1111/j.1525-1314.1993.tb00190.x)
761 [.tb00190.x](http://doi.wiley.com/10.1111/j.1525-1314.1993.tb00190.x) doi: 10.1111/j.1525-1314.1993.tb00190.x
- 762 Mancktelow, N. S. (2008, jun). Tectonic pressure: Theoretical concepts and mod-
763 elled examples. *Lithos*, 103(1-2), 149–177. Retrieved from [https://www](https://www.sciencedirect.com/science/article/pii/S002449370700223X)
764 [.sciencedirect.com/science/article/pii/S002449370700223X](https://www.sciencedirect.com/science/article/pii/S002449370700223X){#}bib83
765 doi: 10.1016/J.LITHOS.2007.09.013
- 766 Martínez-Díaz, J. J. (2002, oct). Stress field variation related to fault interaction
767 in a reverse oblique-slip fault: The Alhama de Murcia fault, Betic Cordillera,
768 Spain. *Tectonophysics*, 356(4), 291–305. doi: 10.1016/S0040-1951(02)00400-6
- 769 Mookerjee, M., & Peek, S. (2014, nov). Evaluating the effectiveness of Flinn’s k-
770 value versus Lode’s ratio. *Journal of Structural Geology*, 68(PA), 33–43. doi:
771 10.1016/j.jsg.2014.08.008
- 772 Moulas, E., Burg, J. P., & Podladchikov, Y. (2014). Stress field associated with el-
773 liptical inclusions in a deforming matrix: Mathematical model and implications
774 for tectonic overpressure in the lithosphere. *Tectonophysics*, 631(C), 37–49.
775 doi: 10.1016/j.tecto.2014.05.004
- 776 Moulas, E., Podladchikov, Y. Y., Aranovich, L. Y., & Kostopoulos, D. (2013,
777 nov). The problem of depth in geology: When pressure does not translate
778 into depth. *Petrology*, 21(6), 527–538. doi: 10.1134/S0869591113060052
- 779 Moulas, E., Schmalholz, S. M., Podladchikov, Y., Tajčmanová, L., Kostopoulos, D.,
780 & Baumgartner, L. (2019). Relation between mean stress, thermodynamic,
781 and lithostatic pressure. *Journal of Metamorphic Geology*, 37(1), 1–14. doi:
782 10.1111/jmg.12446
- 783 Nagel, T. J. (2008, jan). Tertiary subduction, collision and exhumation recorded in
784 the Adula nappe, central Alps. *Geological Society Special Publication*, 298(1),
785 365–392. doi: 10.1144/SP298.17
- 786 Parrish, R. R., Gough, S. J., Searle, M. P., & Waters, D. J. (2006, nov). Plate veloc-
787 ity exhumation of ultrahigh-pressure eclogites in the Pakistan Himalaya. *Geol-*
788 *ogy*, 34(11), 989–992. doi: 10.1130/G22796A.1
- 789 Petrini, & Podladchikov. (2000, jan). Lithospheric pressure-depth relationship
790 in compressive regions of thickened crust. *Journal of Metamorphic Ge-*
791 *ology*, 18(1), 67–77. Retrieved from [http://doi.wiley.com/10.1046/](http://doi.wiley.com/10.1046/j.1525-1314.2000.00240.x)
792 [j.1525-1314.2000.00240.x](http://doi.wiley.com/10.1046/j.1525-1314.2000.00240.x) doi: 10.1046/j.1525-1314.2000.00240.x
- 793 Platt, J. P. (1986, sep). Dynamics of orogenic wedges and the uplift of high-
794 pressure metamorphic rocks. *GSA Bulletin*, 97(9), 1037–1053. doi:
795 10.1130/0016-7606(1986)97<1037:doowat>2.0.co;2

- 796 Pleuger, J., & Podladchikov, Y. Y. (2014). A purely structural restoration of the
797 NFP20-East cross section and potential tectonic overpressure in the Adula
798 nappe (central Alps). *Tectonics*, *33*(5), 656–685. doi: 10.1002/2013TC003409
- 799 Reuber, G., Kaus, B. J., Schmalholz, S. M., & White, R. W. (2016, may). Non-
800 lithostatic pressure during subduction and collision and the formation of
801 (ultra)high-pressure rocks. *Geology*, *44*(5), 343–346. doi: 10.1130/G37595.1
- 802 Ring, U., Brandon, M. T., Willett, S. D., & Lister, G. S. (1999, jan). Exhumation
803 processes. *Geological Society Special Publication*, *154*(1), 1–27. doi: 10.1144/
804 GSL.SP.1999.154.01.01
- 805 Rubatto, D., & Hermann, J. (2001, jan). Exhumation as fast as subduction? *Geol-*
806 *ogy*, *29*(1), 3–6. doi: 10.1130/0091-7613(2001)029<0003:eafas>2.0.co;2
- 807 Rubatto, D., Regis, D., Hermann, J., Boston, K., Engi, M., Beltrando, M., &
808 McAlpine, S. R. (2011, may). Yo-yo subduction recorded by accessory min-
809 erals in the Italian Western Alps. *Nature Geoscience*, *4*(5), 338–342. doi:
810 10.1038/ngeo1124
- 811 Schenker, F. L., Schmalholz, S. M., Moulas, E., Pleuger, J., Baumgartner, L. P.,
812 Podladchikov, Y., ... Müntener, O. (2015, oct). Current challenges for
813 explaining (ultra)high-pressure tectonism in the Pennine domain of the
814 Central and Western Alps. *Journal of Metamorphic Geology*, *33*(8), 869–
815 886. Retrieved from <http://doi.wiley.com/10.1111/jmg.12143> doi:
816 10.1111/jmg.12143
- 817 Schmalholz, S. M., & Podladchikov, Y. (2014). *Metamorphism under stress: The*
818 *problem of relating minerals to depth* (Vol. 42) (No. 8). Geological Society of
819 America. doi: 10.1130/focus0822014.1
- 820 Schmalholz, S. M., & Podladchikov, Y. Y. (2013, may). Tectonic overpressure in
821 weak crustal-scale shear zones and implications for the exhumation of high-
822 pressure rocks. *Geophysical Research Letters*, *40*(10), 1984–1988. Retrieved
823 from <http://doi.wiley.com/10.1002/grl.50417> doi: 10.1002/grl.50417
- 824 Schmalholz, S. M., & Schenker, F. L. (2016, oct). Exhumation of the Dora
825 Maira ultrahigh-pressure unit by buoyant uprise within a low-viscosity man-
826 tle oblique-slip shear zone. *Terra Nova*, *28*(5), 348–355. Retrieved from
827 <http://doi.wiley.com/10.1111/ter.12227> doi: 10.1111/ter.12227
- 828 Schmid, D. W., & Podladchikov, Y. Y. (2003, oct). Analytical solutions for de-
829 formable elliptical inclusions in general shear. *Geophysical Journal Interna-*
830 *tional*, *155*(1), 269–288. doi: 10.1046/j.1365-246X.2003.02042.x
- 831 Schmid, D. W., & Podladchikov, Y. Y. (2005, mar). Mantled porphyroclast gauges.
832 *Journal of Structural Geology*, *27*(3), 571–585. doi: 10.1016/j.jsg.2004.09.005
- 833 Schmid, S. M., Pfiffner, O. A., Froitzheim, N., Schönborn, G., & Kissling, E. (1996,
834 oct). Geophysical-geological transect and tectonic evolution of the Swiss-Italian
835 Alps. *Tectonics*, *15*(5), 1036–1064. doi: 10.1029/96TC00433
- 836 Shao, B., & Hou, G. (2019, apr). The interactions of fault patterns and stress
837 fields during active faulting in Central North China Block: Insights from
838 numerical simulations. *PLOS ONE*, *14*(4), e0215893. Retrieved from
839 <https://dx.plos.org/10.1371/journal.pone.0215893> doi: 10.1371/
840 journal.pone.0215893
- 841 Tajčmanová, L. (2015, oct). Deviations from lithostatic pressure during metamor-
842 phism: fact or fiction? *Journal of Metamorphic Geology*, *33*(8), 783–784. Re-
843 trieved from <http://doi.wiley.com/10.1111/jmg.12152> doi: 10.1111/jmg
844 .12152
- 845 Tajčmanová, L., Podladchikov, Y., Powell, R., Moulas, E., Vrijmoed, J., & Con-
846 nolly, J. (2014, feb). Grain-scale pressure variations and chemical equilibrium
847 in high-grade metamorphic rocks. *Journal of Metamorphic Geology*, *32*(2),
848 195–207. Retrieved from <http://doi.wiley.com/10.1111/jmg.12066> doi:
849 10.1111/jmg.12066
- 850 Tajčmanová, L., Vrijmoed, J., & Moulas, E. (2015, feb). Grain-scale pressure varia-

- 851 tions in metamorphic rocks: implications for the interpretation of petrographic
852 observations. *Lithos*, 216-217, 338–351. doi: 10.1016/j.lithos.2015.01.006
- 853 Townend, J., & Zoback, M. D. (2000, may). How faulting keeps the crust strong:
854 Comment and Reply. *Geology*, 28(5), 399–402. doi: 10.1130/0091-7613(2000)
855 28<399:HFKTCS>2.0.CO
- 856 Wang, K., & Hu, Y. (2006). Accretionary prisms in subduction earthquake cy-
857 cles: The theory of dynamic Coulomb wedge. *Journal of Geophysical Research:*
858 *Solid Earth*, 111(6), 1–16. doi: 10.1029/2005JB004094
- 859 Warren, C. J. (2013, feb). Exhumation of (ultra-)high-pressure terranes:
860 concepts and mechanisms. *Solid Earth*, 4(1), 75–92. Retrieved from
861 <https://www.solid-earth.net/4/75/2013/> doi: 10.5194/se-4-75-2013
- 862 Wheeler, J. (1991, nov). Structural evolution of a subducted continental sliver:
863 The northern Dora Maira massif, Italian Alps. *Journal of the Geological Soci-*
864 *ety*, 148(6), 1101–1113. doi: 10.1144/gsjgs.148.6.1101
- 865 Wheeler, J. (2014, aug). Dramatic effects of stress on metamorphic reactions. *Geol-*
866 *ogy*, 42(8), 647–650. doi: 10.1130/G35718.1
- 867 Yamato, P., & Brun, J. P. (2017, jan). Metamorphic record of catastrophic pressure
868 drops in subduction zones. *Nature Geoscience*, 10(1), 46–50. doi: 10.1038/
869 ngeo2852
- 870 Yang, J. J., Huang, M. X., Wu, Q. Y., & Zhang, H. R. (2014). Coesite-bearing
871 eclogite breccia: Implication for coseismic ultrahigh-pressure metamorphism
872 and the rate of the process. *Contributions to Mineralogy and Petrology*,
873 167(6), 1–17. doi: 10.1007/s00410-014-1013-7